

A gas-surface interaction algorithm for discrete velocity methods in predicting rarefied and multi-scale flows

Jianfeng Chen^a, Sha Liu^{a,b,c,*}, Chengwen Zhong^{a,b,c}, Yong Wang^a, Congshan Zhuo^{a,b,c}, Yanguang Yang^d

^a*School of Aeronautics, Northwestern Polytechnical University, Xi'an, Shaanxi 710072, China*

^b*National Key Laboratory of Science and Technology on Aerodynamic Design and Research, Northwestern Polytechnical University, Xi'an, Shaanxi 710072, China*

^c*Institute of Extreme Mechanics, Northwestern Polytechnical University, Xi'an, Shaanxi 710072, China*

^d*China Aerodynamics Research and Development Center, Mianyang, Sichuan 621000, China*

Abstract

The rarefied flow and multi-scale flow are crucial for the aerodynamic design of spacecraft, ultra-low orbital vehicles and plumes. By introducing a discrete velocity space, the discrete velocity method (DVM) and unified methods can capture complex and non-equilibrium distribution functions and describe flow behaviors exactly. The unified methods predict flows from continuum to rarefied regimes by adopting unified modeling, and they can be further applied to other multi-scale physics such as radiation heat transfer, phonon heat transfer and plasma. In the flow field, the concrete dynamic process needs to describe the gas-gas interaction and gas-surface interaction (GSI). However, in both DVM and unified methods, only a simple but not accurate GSI is used, which can be regarded as a Maxwell GSI with a fixed accommodation coefficient of 1 (full accommodation) at the present stage. To overcome the bottleneck in extending DVM and unified methods to the numerical experiment and investigate real multi-scale flow physics, this paper realizes precise GSI in the DVM framework by constructing the boundary conditions of a concrete Maxwell GSI with an adjustable accommodation coefficient. In the constructing process, the problems

*Corresponding author
Email address: shaliu@nwpu.edu.cn (Sha Liu)

of macro-conservation and micro-consistency in the DVS at the boundary are well solved by reflected macroscopic flux and interpolation distribution function and interpolation error correction, respectively. Meanwhile, considering that the multi-scale flows in the background of aeronautics and aerospace are often at supersonic and hypersonic speeds, the unstructured velocity space (UVS) is essential. From the perspective of generality, the GSI is forced on UVS, while the conventional structured velocity space can be viewed as a special case of UVS. Also, the GSI can be used for both monatomic and diatomic gases with non-equilibrium translational and rotational temperatures (thermal non-equilibrium). Besides, by combined with the unified method (the unified gas-kinetic scheme in the paper), the effectiveness and validity of the present GSI on the DVM framework are verified by flow simulations including supersonic flows over the sharp flat plate in the slip regime, the circular cylinder in the transitional regime, the blunt wedge in the transitional regime, the blunt circular cylinder in the slip regime, and the truncated flat plate in the slip regime.

Keywords: Multi-scale flows; Gas-surface interaction; Accommodation coefficient; Unstructured velocity space

1. Introduction

A deep understanding of rarefied and multi-scale hypersonic flows is critical for the aerodynamic design of spacecraft, ultra-low orbital vehicles and plumes. Usually, the rarefaction degree of gas is quantified by the Knudsen (Kn) number $Kn = \lambda/L$, where λ is the gas mean free path, and L is the characteristic length of the object in the flow. According to the Kn number, the flow can be classified qualitatively into continuum flow ($Kn < 0.001$), slip flow ($0.001 < Kn < 0.1$), transitional flow ($0.1 < Kn < 10$) and free molecular flow ($Kn > 10$). Multi-scale flow is a term with a broad engineering background that refers to the coexistence of different flow regimes. For instance, considering the flow of near-space vehicles and micro-/nano-electro-mechanical systems (MEMS/NEMS), several flow regimes including continuum flow, slip flow, and even free molecule flow

will exist in the same computational domain, and the local Kn number may fluctuate by many orders of magnitude. As essential parts of the flow process, the gas-gas interaction (GGI) and gas-surface interaction (GSI) are handled by flow solvers and boundary conditions, respectively.

1.1 *The numerical methods for flows in all flow regimes.*

In terms of flow numerical prediction, the traditional method of computational fluid dynamics based on Navier-Stokes (N-S) equations is suitable for continuum flows in the airspace and macro scale, whereas the model molecular method based on rarefied gas dynamics, represented by the direct simulation Monte Carlo (DSMC) [1] method, performs well for rarefied flows and micro-scale flows. However, each of the two methods has its difficulties in simulating multi-scale flow numerically [1, 2, 3]. Motivated by the N-S method's and DSMC method's successes in continuum flow and rarefied flow, researchers have combined the two methods through flow-field zoning to address the multi-scale flow problem, and the overlapping hybrid particle-continuum method is proposed [4, 5, 6]. The rarefied computing domain and the continuum computing domain must overlap to improve information transmission. To categorize the flow domain, empirical or semi-empirical criteria are typically used [7, 8]. The multi-scale problem can be partially resolved by the coupling approach, but it is still difficult to split the computational domain precisely and integrate several flow regimes reasonably [2].

In recent years, a class of multi-scale asymptotic preserving (AP) [9] schemes based on kinetic theory have been proposed, making it possible to solve the problem in all flow regimes by using the same numerical method. With a local analytical integral solution to the kinetic model equation for the connected particle transport and collision in the numerical flow, the unified gas-kinetic scheme (UGKS) developed by Xu et al. [10, 11] is a multi-scale technique. Thus, the molecular mean free path and collision time cannot be used as constraints on the size of the cell or the time step. The discrete unified gas-kinetic scheme (DUGKS) proposed by Guo et al. is another multi-scale approach based on

the same physical process as UGKS [12, 13]. Instead of the analytical integral solution, the characteristic difference solution to the kinetic model equation in
45 space and time, which couples the molecular transport and collision effects in a numerical time step, is adopted to reconstruct the multi-scale numerical flux at a cell interface. Therefore, DUGKS can be regarded as a special case of UGKS. After a decade of development, many numerical techniques have been developed and implemented in the UGKS and DUGKS to increase the computational
50 efficiency and reduce memory cost, such as unstructured mesh computation [3, 14], moving grids [15, 2], velocity space adaptation [2], memory reduction [16], wave-particle adaptation [17], implicit algorithms [18, 19, 20], parallelization algorithm [21], and further simplification and modification [22, 23, 24, 25]. With these improvement, the UGKS and DUGKS have been successfully applied to
55 a variety of flow problems in different flow regimes, such as micro flows [26], compressible flows [13, 27], multi-phase flows [28], gas-solid flows [29], and gas mixture systems [30]. Besides flow problems, the UGKS and DUGKS were also extended to multi-scale transport problems such as radiative transfer [31], phonon heat transfer [32], plasma physics [33], neutron transport [34], granular
60 flow [35], and turbulent flow [36, 37].

Because of the wide spreading of the particle velocity distribution in high-speed flows and the narrow-kernel distribution function in cases with a large Kn number, the velocity mesh must cover a huge domain with high resolution. The storage and computational load will be unbearable if a conventional structured
65 velocity mesh is used [38]. The usage of an adaptive velocity mesh in phase space was proposed in the literature [2, 39, 40] to perform automatic velocity mesh revision. However, compared to conventional velocity mesh approaches, adaptive velocity mesh approaches are more challenging and require additional steps in the solution process. Titarev et al. [38] and Yuan et al.[19] provided
70 a relatively simple method for producing a non-uniform unstructured velocity mesh (UVM), and Chen et al. [41, 42] adopted this method for the conserved DUGKS. The benefit of UVM is that it enables flexible grid point placement, which decreases the number of grid points and prevents ray effects.

1.2 The modeling gas-surface interactions and the algorithms.

75 The GSI model's impact increases considerably with gas rarefaction, and it is a primary mechanism that governs aerodynamic forces and heat transmission during hypersonic flight. Therefore, it is crucial to select the right model to calculate hypersonic rarefied flows [43]. The initial and most basic explanation of the GSI model, which consists of the incidence and reflection processes, was
80 provided by Maxwell as early as 1859 [1, 44]. Maxwell established two classical reflection models, namely the specular reflection model and the diffuse reflection model. The two models are the result of a gas molecule colliding with a perfectly reflecting or a completely accommodating solid surface, respectively [45]. In the diffuse reflection model, the gas molecules are adsorbed close to the wall for
85 a considerable amount of time, thus completely erasing any memory of the encounter. These molecules are then uniformly re-emitted to the half-space above the wall at all angles after being desorbed. Based on the macroscopic properties of the solid surface (density, velocity, and temperature), the reflected velocity follows the Maxwell distribution. In the specular reflection model, a gas
90 molecule that directly collides with a wall without being absorbed is reflected like a completely elastic sphere. The normal velocity component is reversible, but the tangential velocity component does not change, and the reflection angle is the same as the incidence angle. The diffuse reflection model is frequently used in natural settings. The time it takes for gas molecules to be adsorbed by the
95 surface, particularly for continuum flows, is typically substantially longer than that for rarefied gas flows or smooth surface flows. Diffuse or specular reflection models should not be used exclusively in situations when the adsorption time is neither very long nor very short. By using the accommodation coefficient σ , Maxwell [46] integrated the diffuse reflection model and the specular reflection
100 model: the incident molecules with a proportion of σ reflect diffusely, while the remaining molecules reflect specularly [43, 45]. Due to this interaction, the Maxwell model is a single-parameter model that cannot describe the transport of momentum and energy simultaneously. Also, the model is difficult to determine since the fraction of diffuse reflection molecules is an empirical metric that highly

105 depends on numerous physical variables of gas and surface [47]. Cercignani and Lampis [48] developed a phenomenological model (CL model) to characterize the GSI in accordance with the reciprocal law, where two parameters pertaining to the tangential momentum and normal energy transport were incorporated. Later, Lord [49, 50] expanded and updated the CL model (known as the CLL
110 model in the DSMC), making it a popular tool for theoretical and computational studies of rarefied gas flows. The CLL model improves the reflected gas molecule velocity distributions and is highly consistent with the lobular distribution, but it is not consistent with the findings of experiments using a molecular beam. Based on the empirical parameters, some models describe the GSI by fitting
115 with the experimental results, among which the Nocilla model [51, 52] and the multi-flux model [53] are the most typical.

Because of its simple implementation, the GSI model in DSMC has drawn much attention [54, 45, 53, 55], but in DVM, the GSI model is less used [56]. Since DVM uses discrete velocity space (DVS), which is fixed in time and space,
120 the specular reflection model can only be applied when the velocity space is symmetrical about the wall boundary. Thus, in a simplified treatment of the previous work, only the diffuse reflection is applied to the flat boundary [56, 57]. Also, it is challenging to establish a DVS that is symmetric for all boundaries because object boundaries are not always straight. Thus, it is necessary to de-
125 velop a boundary condition processing technique that is appropriate for both the general DVM framework and the general boundary shape. The approach proposed in this study is based on the unstructured DVS and is directly transferable to the structured DVS (which can be regarded as a special unstructured DVS). Currently, the Maxwell GSI model, which has a straightforward shape
130 and complies with the reciprocity principle [45], is the most popular model in rarefied gas dynamics. By adjusting the Maxwellian accommodation coefficient, this study investigates how the GSI affects the physical properties of aerodynamic surfaces. Meanwhile, an efficient solver that incorporates the GSI model for all flow regimes is constructed by merging UGKS with a simplified multi-
135 scale flux.

The rest of the paper is organized as follows: in Section 2, the UGKS based on the Boltzmann-Shakhov and Boltzmann-Rykov model equations are introduced. The GSI model based on unstructured DVS is presented in Section 3. Section 4 introduces the numerical simulation and comparison of supersonic
140 flows over the sharp flat plate, circular cylinder, blunt wedge, blunt circular cylinder, and truncated flat plate. Finally, Section 5 concludes this paper.

2. Numerical method

2.1 Gas-kinetic models.

The Boltzmann equation serves as the basis for the UGKS:

$$\frac{\partial f}{\partial t} + \xi \cdot \nabla f = \Omega \quad (1)$$

where $f = f(\mathbf{x}, \xi, \eta, e, t)$ is the velocity distribution functions for particles moving in D-dimensional physical space with a velocity of $\xi = (\xi_1, \dots, \xi_D)$ at position
145 $\mathbf{x} = (x_1, \dots, x_D)$ and time t . Here, $\eta = (\xi_{D+1}, \dots, \xi_3)$ is the dummy velocity (with the degree of freedom $L = 3 - D$) consisting of the remaining components of the translational velocity of particles in three-dimensional space; e is a vector of K elements representing the internal degree of freedom of molecules; Ω is the collision operator. Many kinetic models, including the Bhatnagar-Gross-Krook
150 (BGK) collision model [58], the Shakhov model [59], the ellipsoidal statistical model (ES model) [60], and the Rykov model [61], have been proposed and used in the research of rarefied flows to simplify the collisional model of the full Boltzmann equation. To build kinetic models and develop the corresponding gas-kinetic schemes, numerous attempts have been made. The modeling
155 of monatomic gases only considers the non-equilibrium translational energy. In addition to the three translational degrees of freedom for the diatomic molecule, there are internal degrees of freedom, i.e., two degrees of freedom for rotation at room temperature. The degrees of freedom associated with vibrations begin to
160 arise at a temperature higher than 1000 K. Thus, only the degrees of freedom for translation and rotation are considered in this study, and the UGKS is es-

tablished by using the Shakhov model for monatomic gas and the Rykov model for diatomic gas.

The following presents the expression for the control equation of the Boltzmann-BGK type:

$$\frac{\partial f}{\partial t} + \xi \cdot \nabla f \equiv \Omega = \frac{g^* - f}{\tau} \quad (2)$$

where τ is the relaxation time for the translational degree of freedom and can be calculated as $\tau = \mu/p_t$, where μ and p_t are the viscosity and pressure determined by the translational temperature T_t instead of the equilibrium temperature T . The energy equalization theorem is satisfied by the equilibrium temperature T , the translational temperature T_t , and the rotation temperature T_r . g^* represents the Maxwell equilibrium distribution functions, Shakhov equilibrium distribution functions, or Rykov equilibrium distribution functions. The variable hard sphere (VHS) model is adopted in this study to determine viscosity:

$$\tau = \frac{\mu}{p_t} = \frac{\mu}{\rho R T_t} = \frac{1}{\rho R T_t} \mu_0 \left(\frac{T_t}{T_0} \right)^\omega \quad (3)$$

where ρ and R are the density and the specific gas constant, respectively. The viscosity of the freestream flow μ_0 is correlated with the gas mean free path λ in the following way:

$$\lambda = \frac{2\mu(5-2\omega)(7-2\omega)}{15\rho(2\pi RT)^{1/2}} \quad (4)$$

where T is temperature.

In the non-dimensional system, the Kn number is defined as:

$$Kn = \frac{\lambda}{L_{ref}} = \frac{2\mu(5-2\omega)(7-2\omega)}{15\rho L_{ref}(2\pi RT)^{1/2}} = \sqrt{\frac{\gamma}{\pi}} \frac{\sqrt{2}(5-2\omega)(7-2\omega)}{15} \frac{Ma}{Re} \quad (5)$$

165 where $Ma = \frac{u}{\sqrt{\gamma RT}}$ and $Re = \frac{\rho u L_{ref}}{\mu}$ are the Mach (Ma) number and Reynolds (Re) number, respectively, and L_{ref} is the characteristic length. According to the inter-molecular interaction model, ω is set to 0.5, 0.81, and 0.74 for the hard sphere model, ideal argon, and nitrogen, respectively.

2.2 Reduced gas-kinetic models.

The discrete velocity space should be used to record the free transit of molecules, which is dependent only on the D-dimensional particle velocity ξ

and is not related to η and e (for diatomic gas). The following reduced distribution functions [62] are used in the current numerical scheme to prevent discretizing η and e :

$$\begin{aligned} G(t, \mathbf{x}, \xi) &= m \int f d e d \eta \\ H(t, \mathbf{x}, \xi) &= m \int \eta^2 f d e d \eta \\ R(t, \mathbf{x}, \xi) &= \int e f d e d \eta \end{aligned} \quad (6)$$

The physical meaning of G , H , and R is the distribution of the mass, translational internal energy, and rotating energy in the dummy velocity space and rotational energy space, respectively. The quasi-linear feature of the model equation is advantageous for this condensed treatment. Only the simplified distribution functions G and H are required for monatomic gases. The reduced distribution function R for rotational energy will also be introduced for diatomic gases. Note that R will inevitably vanish in three dimensions. Then, the macro quantity can be expressed as:

$$\mathbf{W} = \begin{pmatrix} \rho \\ \rho \mathbf{u} \\ \rho E \\ \rho E_r \end{pmatrix} = \int \begin{pmatrix} G \\ \xi G \\ \frac{1}{2} (\xi^2 G + H) + R \\ R \end{pmatrix} d\xi \quad (7)$$

where, $\rho E = \rho u^2 + \rho \varepsilon$ is the total energy density, $\rho \varepsilon = \rho c_V T$ is the inertial energy density, and ρE_r is the rotational energy density. The translational heat flux, rotational heat flux, and total heat flux are expressed as:

$$\begin{aligned} \mathbf{q}_t &= \frac{1}{2} \int \mathbf{c} (c^2 G + H) d\xi \\ \mathbf{q}_r &= \int \mathbf{c} R d\xi \\ \mathbf{q} &= \mathbf{q}_t + \mathbf{q}_r \end{aligned} \quad (8)$$

¹⁷⁰ where $\mathbf{c} = \xi - \mathbf{u}$ is the peculiar velocity.

The governing equation of the reduced distribution function is:

$$\begin{aligned}\frac{\partial G}{\partial t} + \xi \cdot \frac{\partial G}{\partial \mathbf{x}} &= \frac{g^G - G}{\tau} \\ \frac{\partial H}{\partial t} + \xi \cdot \frac{\partial H}{\partial \mathbf{x}} &= \frac{g^H - H}{\tau} \\ \frac{\partial R}{\partial t} + \xi \cdot \frac{\partial R}{\partial \mathbf{x}} &= \frac{g^R - R}{\tau}\end{aligned}\quad (9)$$

For diatomic gas flow, the Rykov equilibrium is:

$$\begin{aligned}g^G &= \left(1 - \frac{1}{Zr}\right) G^t + \frac{1}{Zr} G^r \\ g^H &= \left(1 - \frac{1}{Zr}\right) H^t + \frac{1}{Zr} H^r \\ g^R &= \left(1 - \frac{1}{Zr}\right) R^t + \frac{1}{Zr} R^r\end{aligned}\quad (10)$$

with

$$\begin{aligned}G^t &= g^{eq}(T_t) \left[1 + \frac{\mathbf{c} \cdot \mathbf{q}_t}{15p_t RT_t} \left(\frac{c^2}{RT_t} - D - 2\right)\right] \\ G^r &= g^{eq}(T) \left[1 + \omega_0 \frac{\mathbf{c} \cdot \mathbf{q}_t}{15pRT} \left(\frac{c^2}{RT} - D - 2\right)\right]\end{aligned}\quad (11)$$

$$\begin{aligned}H^t &= RT_t g^{eq}(T_t) (3 - D) \left[\left(1 + \frac{\mathbf{c} \cdot \mathbf{q}_t}{15p_t RT_t} \left(\frac{c^2}{RT_t} - D\right)\right)\right] \\ H^r &= RT g^{eq}(T) (3 - D) \left[\left(1 + \omega_0 \frac{\mathbf{c} \cdot \mathbf{q}_t}{15pRT} \left(\frac{c^2}{RT} - D\right)\right)\right]\end{aligned}\quad (12)$$

$$\begin{aligned}R^t &= RT_r \left[G^t + (1 - \delta) \frac{\mathbf{c} \cdot \mathbf{q}_r}{p_t RT_t} g^{eq}(T_t)\right] \\ R^r &= RT \left[G^r + \omega_1 (1 - \delta) \frac{\mathbf{c} \cdot \mathbf{q}_r}{pRT} g^{eq}(T)\right]\end{aligned}\quad (13)$$

g^{eq} represents the Maxwell equilibrium:

$$g^{eq}(T) = \frac{\rho}{(2\pi RT)^{D/2}} \exp\left(-\frac{\mathbf{c}^2}{2RT}\right)\quad (14)$$

where the coefficients are set as [11, 19]: $\delta = 1/1.55$, $\omega_0 = 0.2354$, and $\omega_1 = 0.3049$ for nitrogen in this study. Zr is the rotational relaxation collision number accounting for the ratio of the slower inelastic translation–rotation energy relaxation relative to the elastic translational relaxation.

For monatomic gas flow, the Shakhov equilibrium is:

$$\begin{aligned} g^G &= g^{eq} + G_{Pr} \\ H^G &= H^{eq} + H_{Pr} \end{aligned} \quad (15)$$

with

$$G_{Pr} = (1 - Pr) \frac{\mathbf{c} \cdot \mathbf{q}}{5pRT} \left(\frac{c^2}{RT} - D - 2 \right) g^{eq} \quad (16)$$

$$H^{eq} = (K + 3 - D) RT g^{eq} \quad (17)$$

$$H_{Pr} = (1 - Pr) \frac{\mathbf{c} \cdot \mathbf{q}}{5pRT} \left[\left(\frac{c^2}{RT} - D \right) (K + 3 - D) - 2K \right] RT g^{eq} \quad (18)$$

175 where the Prandtl (Pr) number equals 2/3. All the above equilibrium distribution functions can be obtained by macroscopic quantities.

2.3 UGKS with simplified multi-scale flux.

In this study, the distribution function and macro quantity of the UGKS with simplified multi-scale flux are updated simultaneously. Before updating 180 the micro-distribution function, the macro-quantity is updated first, followed by the equilibrium distribution function. For traditional flow field output, macro-quantities and other statistics are used.

For the sake of simplicity, G , H , and R can be replaced with the new symbol ϕ in the algorithm because they share the same updating process, as shown in Eq. (9). Then, the governing equation can be rewritten as:

$$\frac{\partial \phi}{\partial t} + \xi \cdot \nabla \phi = \Omega_\phi \equiv \frac{g^\phi - \phi}{\tau} \quad (19)$$

Integrating Eq. (19) into control volume V_j from time t_n to t_{n+1} yields:

$$\phi_j^{n+1}(\xi) - \phi_j^n(\xi) + \frac{\Delta t}{|V_j|} F_j^{n+1/2}(\xi) = \frac{\Delta t}{2} [\Omega_j^{n+1}(\xi) + \Omega_j^n(\xi)] \quad (20)$$

where $|V_j|$ and $\Delta t = t_{n+1} - t_n$ denote the volume of V_j and the time interval; F_j^{n+1} denotes the microflux across the cell interface, and it is determined by:

$$F_j^{n+1/2}(\xi) = \int_{\partial V_j} (\xi \cdot \mathbf{n}_f) \phi(\mathbf{x}_f, \xi, t_{n+1/2}) dS \quad (21)$$

where ∂V_j is the surface of the control volume V_j , and \mathbf{x}_f and \mathbf{n}_f are the interface's midpoint and the external normal unit vector of dS (an infinitesimal element of ∂V_j), respectively. It should be noted that a trapezoidal rule is
185 adopted for the time discretization of the collision term.

In this study, Eq. (20) is integrated into the velocity space to update the conservative variables [63, 41]:

$$\mathbf{W}_j^{n+1} = \mathbf{W}_j^n - \frac{\Delta t}{|V_j|} \int \int_{\partial V_j} (\xi \cdot \mathbf{n}_f) \begin{pmatrix} G(\mathbf{x}_f, \xi, t_{n+1/2}) \\ \xi G(\mathbf{x}_f, \xi, t_{n+1/2}) \\ \frac{1}{2} [\xi^2 G(\mathbf{x}_f, \xi, t_{n+1/2}) + H(\mathbf{x}_f, \xi, t_{n+1/2})] \\ R(\mathbf{x}_f, \xi, t_{n+1/2}) \end{pmatrix} dS d\xi + S \quad (22)$$

where $S = (0, 0, 0, S_r)^T$ is the source term, and only the rotation term is not zero:

$$S_r = \frac{\Delta t}{2} \int [\Omega_r^n + \Omega_r^{n+1}] d\xi = \frac{\Delta t}{2Z_r \tau^n} ([\rho RT]^n - [\rho RT_r]^n) + \frac{\Delta t}{2Z_r \tau^{n+1}} ([\rho RT]^{n+1} - [\rho RT_r]^{n+1}) \quad (23)$$

Afterward, the implied evolution shown in Eq. (20) can be changed into the following explicit equation:

$$\phi_j^{n+1}(\xi) = \left(1 + \frac{\Delta t}{2\tau_j^{n+1}}\right)^{-1} \left[\phi_j^n(\xi) - \frac{\Delta t}{|V_j|} F_j^{n+1/2}(\xi) + \frac{\Delta t}{2} \left(\frac{g_j^{\phi, n+1}(\xi)}{\tau_j^{n+1}} + \frac{g_j^{\phi, n}(\xi) - \phi_j^n(\xi)}{\tau_j^n} \right) \right] \quad (24)$$

The evolution equations for the microscopic distribution functions and the macroscopic conservative variables are shown in Eqs. (22) and (24), respectively. The entire scheme may be established after the distribution functions
190 $\phi(\mathbf{x}_f, \xi, t_{n+1/2})$ at the cell interface are obtained.

The origin UGKS and DUGKS use analytic and numerical quadrature solutions respectively to obtain $\phi(\mathbf{x}_f, \xi, t_{n+1/2})$. In this study, the simplified multi-scale flux is built by using the numerical quadrature solution. The characteristic line (in the direction of particle velocity) is integrated by using Eq. (19) from t_n to $t_{n+1/2}$. The characteristic line ends at the midpoint of the cell interface, as shown in Fig. 1. This procedure is described by the following

equation:

$$\phi(\mathbf{x}_f, \xi, t_n + h) - \phi(\mathbf{x}_f - \xi h, \xi, t_n) = h \frac{g^\phi(\mathbf{x}_f, \xi, t_n + h) - \phi(\mathbf{x}_f, \xi, t_n + h)}{\tau^{n+1/2}} \quad (25)$$

where $h = \frac{\Delta t}{2}$ denotes a half-time step, and \mathbf{x}_f denotes the midpoint of the interface. Finally, the interface distribution function $\phi(\mathbf{x}_f, \xi, t_{n+1/2})$ can be expressed as:

$$\phi(\mathbf{x}_f, \xi, t_n + h) = \frac{\tau^{n+1/2}}{\tau^{n+1/2} + h} \phi(\mathbf{x}_f - \xi h, \xi, t_n) + \frac{h}{\tau^{n+1/2} + h} g^\phi(\mathbf{x}_f, \xi, t_n + h) \quad (26)$$

where $\phi(\mathbf{x}_f, \xi, t_n + h)$ can be integrated into the velocity space to produce the macroscopic quantity at the new moment, on which $g^\phi(\mathbf{x}_f, \xi, t_n + h)$ depends. Meanwhile, $\phi(\mathbf{x}_f - \xi h, \xi, t_n)$ can be calculated from the following reconstruction through the Taylor expansion at the control volume:

$$\phi(\mathbf{x}_f - \xi h, \xi, t_n) = \phi_C(\mathbf{x}_C, \xi, t_n) + \Psi(\mathbf{x}_C, \xi, t_n) \nabla \phi_C(\mathbf{x}_C, \xi, t_n) \cdot (\mathbf{x}_f - \xi h - \mathbf{x}_C), \mathbf{x}_f - \xi h \in V_C \quad (27)$$

where V_c represents the control volume which is centered at point C (Fig. 1). If $\xi \cdot \mathbf{n}_f \geq 0$, point C is P (the center of the left cell) in Fig. 1; otherwise, point C is Q (the center of the right cell). $\phi_C(\mathbf{x}_C, \xi, t_n)$ is the gradient of the auxiliary distribution functions at point C, which is calculated by the least-square method in this study, and $\Psi(\mathbf{x}_C, \xi, t_n)$ is the gradient limiter used to suppress the numerical oscillations. Besides, the Venkatakrishnan limiter [64] is chosen in this paper.

3. Maxwellian boundary condition in unstructured DVS

For solid wall flows, the discrete distribution functions at the wall surface should be given under the proper wall boundary conditions, such as the GSI model [65]. The most widely used model is the Maxwell model, which is based on classical thermodynamics and assumes that molecules will either reflect diffusely with complete energy accommodation or reflect specularly with no change

in energy [54]. The fraction of molecules that will be scattered diffusely is specified by the accommodation coefficient σ , and the distribution function of the reflection from the wall to the flow field is described as:

$$\phi(\mathbf{x}_w, \xi, t^n + h) = \sigma \phi^{eq}(\xi; \rho_w, \mathbf{u}_w, T_w) + (1 - \sigma) \phi(\mathbf{x}_w, \xi, t^n + h), \quad \xi \cdot \mathbf{n}_w < 0 \quad (28)$$

where \mathbf{x}_w , \mathbf{u}_w , T_w , and \mathbf{n}_w are respectively the center position, velocity, temperature, and unit normal vector of the wall, and the direction of \mathbf{n}_w is opposite to the flow field. The distribution functions of diffuse and specular reflections are $\phi^{eq}(\xi; \rho_w, \mathbf{u}_w, T_w)$ and $\phi(\mathbf{x}_w, \xi, t^n + h)$, respectively.

3.1 Diffuse-scattering boundary condition.

The diffuse reflection model, also referred to as the diffuse-scattering rule, is a general boundary condition that presupposes the distribution function for the reflected molecules following the Maxwellian one. The i -th reflection distribution function at the half-time step $t^n + h$ is given as:

$$\phi(\mathbf{x}_w, \xi_i, t^n + h) = \phi^{eq}(\xi_i; \rho_w, \mathbf{u}_w, T_w), \quad \xi_i \cdot \mathbf{n}_w < 0 \quad (29)$$

In this case, the wall density ρ_w should be solved according to the non-penetration criterion:

$$\sum_{\xi_i \cdot \mathbf{n}_w < 0} w_i(\xi_i \cdot \mathbf{n}) \phi^{eq}(\xi_i; \rho_w, \mathbf{u}_w, T_w) + \sum_{\xi_i \cdot \mathbf{n}_w > 0} w_i(\xi_i \cdot \mathbf{n}) \phi(\mathbf{x}_w, \xi_i, t^n + h) = 0 \quad (30)$$

Since Eq. (26) can be used to derive the wall incidence distribution function, the wall density can be also derived:

$$\rho_w = - \sum_{\xi_i \cdot \mathbf{n}_w > 0} w_i(\xi \cdot \mathbf{n}) \phi(\mathbf{x}_w, \xi, t^n + h) / \sum_{\xi_i \cdot \mathbf{n}_w < 0} w_i(\xi \cdot \mathbf{n}) \phi^{eq}(\xi; 1, \mathbf{u}_w, T_w) \quad (31)$$

3.2 Specular reflection boundary condition.

The fundamental principle of specular reflection points out that when a gas molecule's reflection angle equals its incidence angle, it is reflected like an ideal sphere with its normal velocity component being inverted and the tangential

velocity component remaining constant. If the discrete velocity mesh is asymmetric about the wall, it will be difficult for the reflection gas molecules to land on a particular discrete velocity mesh point for DVM. In this case, it is necessary to interpolate the distribution function to achieve macroscopic conservation (i.e., no mass and energy passing through the wall) and microscopic consistency. As shown in Fig. 2, the DVS points used for the flow field are represented by the solid dots. Without losing generality, if the wall is horizontal (represented by the horizontal solid line in the figure), the discrete velocity point in the incident region (below the solid line) is the solid point (here, the point is the distribution function of the molecules shot at the wall), and its corresponding mirror point (corresponding to the distribution function of the mirrored reflected molecules) is the hollow point in the reflection region (above the solid line). Thus, the incident point ξ_i and the wall normal vector \mathbf{n}_w can be exploited to determine the position of the mirror point ξ'_i in the velocity space:

$$\xi'_i = \xi_i - 2\mathbf{n}_w \cdot (\xi_i \cdot \mathbf{n}_w) \quad (32)$$

205 The incident distribution function is shown in Eq. (26), so it is possible to determine the distribution function of the solid points in the lower half of Fig. 2. Meanwhile, the distribution function of the mirror points or hollow points in the upper half of the region has a value equal to that of the solid points. Then the reflected distribution functions of the solid points in the reflection region, 210 i.e., the real velocity points of the current velocity mesh, can be obtained by reconstructing the spatial points nearby while guaranteeing the accuracy (conservation) of the flux integral. It is important to keep in mind that extrapolation should be avoided when performing spatial interpolation. When interpolation cannot be done, one can utilize the zero-order approximation. The reflected 215 macroscopic flux as well as the reflection distribution function must both meet the specular reflection boundary condition. Because the Maxwellian GSI on the DVM is first proposed in this study, two efficient methods for reflected macroscopic flux are offered.

3.2.1 Method 1 for calculating reflected macroscopic flux

This study first finds a sufficient number of hollow points (with an unknown distribution function) close to the solid points (with a known distribution function) in the reflection region. This enables the calculation of the distribution function value of the solid points in the reflection region or the distribution function value of the reflection. Meanwhile, the microscopic flux must be numerically integrated into the DVS because the macroscopic flux at the interface and boundary update the cell-centered conserved values in UGKS. In this case, the question of integration weights arises. If the weights of these hollow points are still determined based on the size of the velocity space mesh, there will be a problem with the non-conservation of macroscopic flux on the boundary, and the weights must be changed to solve this problem. In this study, the reflection distribution function is established for the specular reflection boundary through interpolation, and its initial integral weights must be rebuilt because they are no longer relevant. It is still assumed that the wall is horizontal (horizontal solid line in the figure), the discrete velocity point in the incident region is solid (below the solid line), and its corresponding mirror point is hollow (in the reflection region), as shown in Fig. 3 (above the solid line). By using the law of conservation of mass, momentum, and energy, the solid point in the reflection region can be spatially interpolated to determine the value of the distribution function. Then, the set of weight equations for the i -th discrete velocity can be derived:

$$\varphi_{i,o}\phi_{i,o}w_{i,o}(\xi_i \cdot \mathbf{n}_w) = \sum_{k=1}^n \varphi_{i,k}\phi_{i,k}w_{i,k}(\xi_i \cdot \mathbf{n}_w) \quad (33)$$

220 where $\varphi = [1, \xi, \frac{1}{2}\xi^2]^T$ represents collision invariant; φ_i , ϕ_i , and w_i represent
the mass, momentum, and energy of the i -th incident velocity point. The in-
formation about the hollow point (the mirror point of the incident point) and
the k -th solid point (the reflected point) around the hollow point is provided
by the subscripts o and k , respectively. It should be noted that in Eq. 33, only
225 the integral weight at the right end of the equal sign is unclear. To establish
the appropriate set of equations, it is necessary to select a sufficient number

of neighboring points. The equation implies that the contribution of a single mirror point (incident point) is equal to that of many reflected points. Then, the integral weights of the reflected points must be added once all mirror points (incident points) have been decomposed equally.

3.2.2 Method 2 for calculating reflected macroscopic flux

For specular reflections, the flux information of the incident distribution function in conjunction with the wall physical parameters can be used directly to accurately and reliably estimate the macroscopic flux of the reflected molecules. The velocity-space weights must be uniform throughout the flow field without further weight modification. In this study, the moments of the incident distribution function are employed to determine the incident flux of mass, momentum, and energy. Then, the reflected flux are obtained directly by using the conservation of mass, momentum, energy, constant tangential momentum flux, and reverse normal momentum flux of the specular reflection condition. This is another method for solving the wall reflected macroscopic flux. Denote the macroscopic incident flux and reflected flux as \mathbf{F}^I and \mathbf{F}^R respectively. Then, we have:

$$\begin{aligned}
 F_{\rho}^I &= -F_{\rho}^R \\
 F_{\rho E}^I &= -F_{\rho E}^R \\
 F_{\rho U}^I &= -[(1 - 2n_x^2) F_{\rho U}^R + (-2n_x n_y) F_{\rho V}^R] \\
 F_{\rho V}^I &= -[(-2n_x n_y) F_{\rho U}^R + (1 - 2n_y^2) F_{\rho V}^R]
 \end{aligned} \tag{34}$$

where F_{ρ} , $F_{\rho E}$, $F_{\rho U}$, and $F_{\rho V}$ represent the flux of mass, energy, x-directional, and y-directional momentum, respectively. Since Method 1 requires the solution of a system of equations, whereas Method 2 does not, so Method 2 is preferred over Method 1.

3.2.3 Micro-consistency

Interestingly, both Methods 1 and 2 are based on the constancy of the macroscopic flux. The distribution function of the reflection region is interpolated in

the velocity space at the microscopic level, which leads to an interpolation error:

$$\phi_{int} = \phi_{re} + \phi_{err}, \quad \xi_i \cdot \mathbf{n}_w < 0 \quad (35)$$

where the interpolated distribution function (denoted as ϕ_{int}) is the sum of the actual reflection distribution function (denoted as ϕ_{re}) and the deviation distribution function (denoted as ϕ_{err}). The divergence of the interpolation distribution function causes the microscopic flux of the wall cells to vary, which in turn causes the cell-centered distribution function (a microscopic update produced by updating the next step) to vary. Since the conserved flux conforms to the specular reflection boundary condition, the cell-centered macroscopic variables can be exploited to adjust the cell-centered distribution function and ensure the conservation:

$$f^{n+1} = \bar{f}^{n+1} + g(\mathbf{W}^{n+1}) - \bar{g}(\bar{\mathbf{W}}^{n+1}) \quad (36)$$

where $\bar{\mathbf{W}}^{n+1}$ is the conserved quantity determined poorly by integrating the cell-central distribution function, and \mathbf{W}^{n+1} is the conserved quantity determined by accurately updating the conserved flux. In numerical simulations of the supersonic flow across a cylinder, it was found that if no error correction was applied to distribution function interpolation, the simulation process would crash immediately, and after the correction, precise results could be obtained.

The basic idea of the approach proposed in this study is the interpolation of the reflection distribution function while ensuring the conservation of macroscopic flux and the consistency of microscopic flux. Here, the Maxwellian boundary condition is applied to the unstructured velocity space.

4. Numerical experiment

In this section, a series of examples, including monatomic and diatomic flows, are used to demonstrate the extended application of the GSI model to the unstructured DVS.

4.1 Verification of monatomic flows.

4.1.1 Supersonic flow over a sharp flat plate.

To evaluate the accuracy of the GSI model in monatomic UGKS, the first numerical simulation considers a monatomic gas supersonic flow passing a sharp flat plate. Though the simulated gas utilized in this configuration is a hard sphere gas, it is based on the wind tunnel test run34 conducted by Tsuboi and Matsumoto[66]. Fig. 4(a) presents the physical mesh used for calculation and the flat plate's geometric shape. The front end of the flat plate has a sharp angle of 30 degrees, a thickness of 15 mm, and an upper surface length of 100 mm. The surface temperature of the flat plate is 290K, whereas the freestream is a hypersonic flow of the argon gas at a Ma number of 4.89 with a temperature of 116 K. The Kn number for the freestream with the plate's length as characteristic length is 0.0078. The unstructured velocity mesh under simulation has 896 cells, as shown in Fig. 4(b).

When σ equals to 1, a completely diffuse reflection is indicated, and the distribution of pressure, shear stress, and heat flux on the wall are shown in Fig. 5. In this case, the calculation results in this study closely match those of DS2V. In the comparison of the variables on the solid wall for the flat plate simulation, the horizontal coordinate is S , and the trailing edge of the flat plate's upper surface serves as the starting point in this coordinate. The distribution of pressure, shear stress, and heat flux on the wall at $\sigma=0.8$ are illustrated in Fig. 6. The distribution of pressure, shear stress, and heat flux on the wall at $\sigma=0$, i.e., the complete specular reflection, are shown in Fig. 7. The comparison of these results indicates that the Maxwell-GSI model based on the unstructured discrete velocity mesh is accurate and fits well with the combination of DS2V calculations. The density, temperature, and horizontal velocity contours for diffuse reflection and specular reflection from the simulation are shown in Fig. 8 and Fig. 9, respectively. It is visible that the specular reflection boundary, which differs greatly from the diffuse reflection boundary, is comparable to the inviscid boundary and has no hysteresis impact on the tangential flow. The distribution function contours on the top surface and the bevel of the flat plate were also monitored, as illustrated in Fig. 10 and Fig. 11. The distribution

function for a diffuse reflection wall follows the Maxwell distribution, while the reflection distribution function for a specular reflection wall is symmetric with the incidence distribution function about the boundary. To further investigate the impact of the GSI model during the change from complete diffuse reflection to complete specular reflection, Fig. 12 presents the distribution of physical quantities on the flat plate's surface for σ values of 1, 0.8, 0.6, 0.4, 0.2, and 0, respectively.

4.1.2 Mach 5 rarefied gas flow over a circular cylinder.

The second simulation simulates a hypersonic flow through a circular cylinder, and it aims to demonstrate the GSI model's applicability to curved surface boundaries. The freestream has a Ma number and Kn number of 5.0 and 1.0, respectively. Argon serves as the working gas, and a variable hard sphere molecular model is employed. The specific heat ratio and the Prandtl number are 5/3 and 2/3, respectively. The temperature of the freestream is 273 K, and the velocity is 1539.3 m/s as a result. Freestream has a dimensionless density, temperature, and velocity of 1.0, 1.0, and 4.56, respectively, while the wall's dimensionless temperature remains constant at 1.0. The computational domain is discretized into 64x61 control bodies and is a circular region with a circle center at (0,0) and a radius of 15. The wall mesh quality must meet specific criteria to accurately depict the heat flux on the cylindrical surface. In this illustration, the first mesh height of the circular surface is 0.01. The unstructured discrete velocity mesh used in this example has 2391 cells, as shown in Fig. 13.

As shown in Fig. 14, on the stationary line in front of the cylinder is the distribution of density, pressure, temperature, and horizontal velocity when σ is 1. It can be observed that the results of UGKS and DSMC are highly consistent with all of the current calculations. As a result of the Shakhov model, the distribution of temperature on the stationary line is slightly higher than the DSMC results prior to the bow shock, which is consistent with the phenomenon described in the literature [67] in the shock wave structure. When σ is 1, Fig. 15 shows the distribution of pressure, shear stress, and heat flux on the cylinder's

surface. All of the calculated results are in perfect agreement with those of
 UGKS and DSMC. As shown in Fig. 16, on the stationary line in front of
 315 the cylinder is the distribution of density, pressure, temperature, and horizontal
 velocity when σ is 0.8. When σ is 0.8, Fig. 17 shows the distribution of pressure,
 shear stress, and heat flux on the cylinder's surface. As shown in Fig. 16, on the
 stationary line in front of the cylinder is the distribution of density, pressure,
 temperature, and horizontal velocity when σ is 0. When σ is 0, Fig. 17 shows
 320 the distribution of pressure, shear stress, and heat flux on the cylinder's surface.
 It can be seen that the calculated results under various σ closely correspond to
 the results of the DSMC. At various σ , the distribution of pressure, shear stress,
 and heat flux on the cylinder's surface is presented in Fig. 20. It is discovered
 that the results of the hypersonic cylinder flow are affected to varying degrees
 325 by the GSI model accommodation coefficients. The wall does not change the
 tangential motion of the gas molecules when the GSI model is treated as total
 specular reflection, which is very similar to the inviscid flow. The pressure at
 the front of the cylinder at $\sigma=0$ is higher than that at $\sigma=1$. This is because the
 normal motion of the gas molecules is completely reflected back, which is similar
 330 to the wall applying a stronger force to the gas molecules than that in the case of
 completely diffuse reflection. The comparison of the drag coefficients at various
 σ is shown in Table 1. The drag coefficients calculated in the paper and the
 DS2V calculation are very similar. Pressure and friction together produce the
 drag force on the cylinder. The drag coefficient of the cylinder in the current
 335 arrangement does not change significantly under different σ , indicating that the
 wall pressure increases and the wall shear stress decreases as σ decreases. Later
 research will investigate the impact of the GSI model on the cylinder's resistance
 at various Kn .

4.1.3 Hypersonic flow over a blunt wedge.

340 It is crucial to accurately predict the hypersonic bottom flow for near-space
 vehicles, particularly when Reaction Control System (RCS) is installed on the
 bottom of some vehicles. Also, it is essential to evaluate the effectiveness of

Table 1: The drag coefficients of cylinder.

σ	Present	DS2V	Relative Error
1	1.925	1.917	0.42%
0.8	1.914	1.910	0.26%
0.6	1.910	1.912	-0.10%
0.4	1.912	1.924	-0.62%
0.2	1.921	1.946	-1.28%
0	1.938	1.970	-1.62%

the RCS and the reach of the jet's effects. The current approach evaluates the effectiveness for the high supersonic dilute expansion flow by simulating the hypersonic flow over a blunt wedge with reference to the configuration in the literature [68]. Fig. 21 presents the geometry of the blunt wedge, which has a length of $L=120$ mm, a head radius of $R=20$ mm, a bottom height of $H=74.72$ mm, and a body slope of $\theta=10^\circ$. A VHS model with argon as the working gas is used here. Meanwhile, the Ma number of freestream is 8.1, the angle of attack is 0° , the temperature is 189 K (equivalent to an altitude of 85 Km), the wall temperature is 273 K, and the Kn number with R and H as the characteristic length is 0.338 and 0.090, respectively. In this simulation, the unstructured physical mesh has 11905 cells, and the unstructured velocity mesh has 3056 cells, as shown in Figs. 22(a) and 22(b), respectively.

The pressure, shear stress, and heat flux distribution over the surface of the blunt wedge at $\sigma=1$ are illustrated in Fig. 23, and the results are contrasted with those of UGKS and DS2V. $0 < s < 27.9$ denotes the wedge's head arc, $27.9 < s < 132.9$ denotes the wedge's body, and $132.9 < s < 170.3$ denotes the wedge's bottom. The comparison results indicate that the findings of this study are highly consistent with those of UGKS and DS2V. Even the variables at the bottom of the wedge, which are two or three orders of magnitude lower than the stationary location, can be predicted with high precision. The results of pressure, shear stress, and heat flux on the blunt wedge surface with DS2V for

0.8 and 0 are shown in Figs. 24 and 25, respectively. It can be observed that the
365 simulation results are in good agreement with those of DS2V. The calculation
results at different σ are combined and compared to investigate the impact of
the GSI model on the physical properties of the blunt wedge object surface, and
the results are presented in Fig. 26. It can be seen that the impact of the GSI
model is more significant on the shear stress and heat flux in the blunt wedge
370 head.

4.2 Verification of diatomic flows.

4.2.1 Supersonic flow around a blunt circular cylinder.

Here, the diatomic gas flow is simulated by considering the degrees of freedom
for translation and rotation of molecules. The accuracy of the GSI model in the
375 diatomic UGKS is validated by this simulation. With a freestream Ma number
of 5.0 and a Kn number of 0.1 (taking the cylinder's radius as the characteristic
length), a supersonic flow around a blunt circular cylinder was simulated. The
temperature of the freestream is 273 K, and the velocity is 1684.6 m/s as a
result. The physical mesh and the unstructured discrete velocity mesh used in
380 the simulation have 9480 cells and 1620 cells respectively, as shown in Fig. 27.
A semicircle with a radius of 1.0 and the center coordinate at (0,0) makes up
the front end of the obtuse body. The height of the initial mesh layer is 0.005,
and the semicircle is divided into 100 and 79 cells in the circumferential and
radial directions, respectively. The working gas for this simulation is nitrogen,
385 and a VHS model is used. The freestream dimensionless density, temperature,
and velocity are 1.0, 1.0, and 4.1833, respectively, and the wall dimensionless
temperature is 1.0.

The distributions of pressure, shear stress, and heat flux over the object's
surface at $\sigma=1$, 0.8, and 0 are shown in Figs. 28, 29, and 30, respectively. It
390 can be seen that the results of this study closely match those of DS2V. The
distribution of physical quantities on the surface of the object at various σ is
presented in Fig. 31, which indicates that the GSI model significantly affects
the distribution of shear stress and heat flux on the wall.

4.2.2 Rarefied hypersonic flow over a truncated flat plate.

395 The comparison of experimental results helps to confirm the effectiveness of the method proposed in this paper because the previous instances are compared with numerical results. Rarefied hypersonic flow over flat plates has been studied theoretically, experimentally, and numerically by many researchers, such as [69, 70, 71]. The simplicity of the geometry and the precision of experimental results
400 make this case particularly useful for numerical validation. Here, the rarefied hypersonic flow over a flat plate with a truncated leading edge is investigated.

Allegre et al. [70] initially conducted this experiment and the freestream conditions given in Table 2 were used. In this experimental study, a truncated flat plate was positioned at a distance from a nozzle producing a nitrogen flow with a Ma number of 20.2 and a temperature of 13.32 K (the gas constant of nitrogen is $R_{N_2} = 297 J / (kg \cdot K)$). The plate is 100 mm long, 100 mm wide, and 5 mm thick, and the wall temperature was maintained at 290 K. Two angles of attack (0° and 10°) were examined in this experiment. The experimental measurements of pressure, heat flux, and density were found to have errors of 15%, 10%, and 10% respectively [72]. By using the VHS ($\omega = 0.74$) model, the gas mean free path is represented as:

$$\lambda_\infty = \frac{1}{\sqrt{2}\pi d_{ref}^2 n_\infty} \left(\frac{T_\infty}{T_{ref}} \right)^{\omega-1/2} \quad (37)$$

The molecular diameter and relative molecular mass of nitrogen are 4.17×10^{-10} m and 4.65×10^{-26} g, respectively. As a result, the molecular gas mean free path and the number density are 0.00169 m and 3.713×10^{20} \cdot /m^3 , respectively.
405 Meanwhile, by using the length of the plate (100 mm) as the characteristic length, the corresponding Kn number is 0.0169. The reference physical quantities and dimensionless physical quantities are presented in Tables 3 and 4, respectively.

The unstructured physical mesh and velocity mesh used for the numerical
410 experiments consist of 8055 and 3186 cells, as depicted in Figs. 32(a) and 32(b), respectively. To investigate the effect of the GSI model on the simulation results in this example, the accommodation coefficient was given only two values of 1

Table 2: Freestream conditions for flat-plate simulations.

Parameter	Value	Unit
Velocity(V_∞)	1503	m/s
Temperature(T_∞)	13.32	K
Density(ρ_∞)	1.727×10^{-5}	kg/m
Pressure(p_∞)	0.0683	Pa

and 0.8 (this value corresponds to literature prescriptions for a nitrogen flow over a steel plate at temperature $T_w = 300$ K [73, 74, 75]). Figs. 33 and 34 show the simulated pressure and heat flux distribution on the lower surface of the flat plate at 0 and 10 degrees of attack angle, respectively. The results obtained by both the DSMC and the proposed method with $\sigma=0.8$ at an attack angle of 0 degrees are more consistent with the experimental results than those at $\sigma=1$, and the simulation results of the proposed method agree with the experimental results more favorably than the DSMC results. However, for the attack angle of 10 degrees, a different phenomenon can be observed. Although the results of the proposed method at $\sigma=0.8$ are closer to the experimental values than those at $\sigma=1$, the DSMC results for the pressure distribution are in better agreement with the experimental values. Meanwhile, the results of the proposed method more closely match the experimental values for the heat flux distribution under $\sigma=1$ at the leading edge of the plate than those under $\sigma=0.8$. Overall, these numerical experiment results show that the GSI model with an adjustable adaption factor should be used because it is more reasonable and obtains results closer to the experimental values than the results at $\sigma=1$.

5. Conclusion

The specular reflection boundary, a crucial component of the GSI model, is resolved in this study, and the Maxwell GSI model is applied for the first time to the DVM framework to extend its application to all flow regimes. Since the velocity mesh is not symmetric about the wall boundary for every geometry

Table 3: Reference physical quantities.

Parameter	Value	Unit
Velocity(V_{ref})	$\sqrt{2R_{N_2}T_\infty}$	m/s
Temperature(T_{ref})	T_∞	K
Density(ρ_{ref})	ρ_∞	kg/m
Length(L_{ref})	1	mm

Table 4: Dimensionless physical quantities.

Parameter	Value
Velocity(V)	16.9
Temperature(T)	1
Density(ρ)	1
Pressure(p)	0.5
Length(p)	100

435 shape, it is difficult to calculate the values of the specular reflection distribution
 functions and determine whether the reflection macroscopic flux satisfies the
 specular reflection requirement. In this study, two methods are used to calcu-
 late the reflected macroscopic flux to ensure macro-conservation, while interpo-
 lation distribution function and interpolation error correction are employed to
 440 ensure micro-consistency. Additionally, the method in this study is directly de-
 veloped with the unstructured DVS because it is essential for hypersonic flows.
 Numerical simulations show that the proposed method is accurate and effec-
 tive. Also, the weight of complete diffuse reflections and specular reflections,
 or the accommodation coefficient σ in the GSI model have a significant impact
 445 on the aerodynamic forces and heat transfer of the flow in numerical predic-
 tions. Besides, The use of completely diffuse reflection boundary conditions is
 not accurate enough, especially for rarefied and multi-scale flows.

The examples presented in this study are all 2-dimensional, but the main idea
 of the method can be applied to any case, and the application of 3-dimensional

450 examples will be discussed in our future work.

Acknowledgments

The authors thank Prof. Kun Xu in the Hong Kong University of Science and Technology and Prof. Zhaoli Guo in Huazhong University of Science and Technology for discussions of the UGKS, the DUGKS and multi-scale flow simu-
455 lations. Jianfeng Chen thanks Dr. Ruifeng Yuan in Northwestern Polytechnical University for useful discussions on the unstructured velocity space. Jianfeng Chen thanks researcher/Dr. Dingwu Jiang in the China Aerodynamics Research and Development Center and Dr. Hao Jin in Northwestern Polytechnical Uni-
460 versity for their help in the use of DS2V. Sha Liu thanks Prof. Fang Ming, Prof. Bi Lin and Prof. Tu Guohua in the China Aerodynamics Research and Development Center for discussions of effective boundary conditions in rarefied flows. This work was supported by the National Natural Science Foundation of China (Grant Nos. 12172301, 11902266, 12072283, and 11902264) and the 111 Project of China (Grant No. B17037). This work is supported by the high
465 performance computing power and technical support provided by Xi'an Future Artificial Intelligence Computing Center.

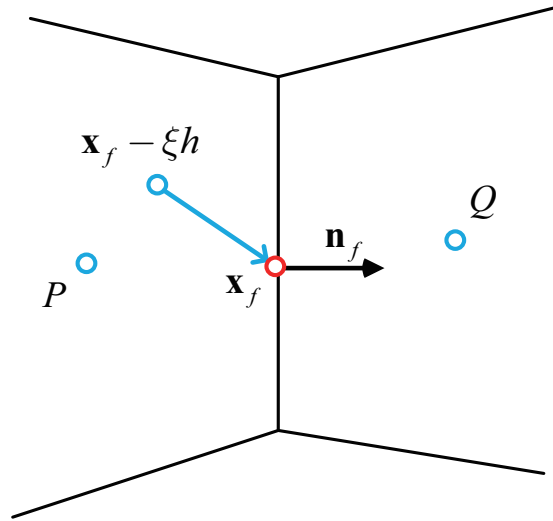


Figure 1: The sketch of two neighboring cells and the characteristic-line.

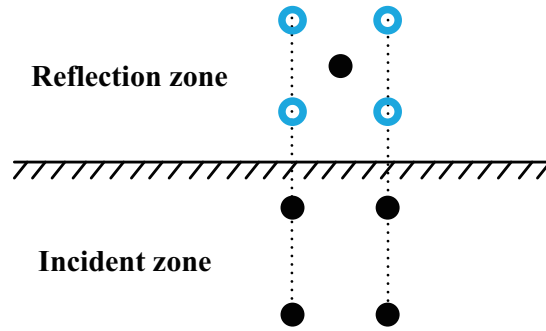


Figure 2: Templates for distribution function interpolation (the solid points represent discrete velocity points, and the hollow points represent mirror points of discrete velocity points).

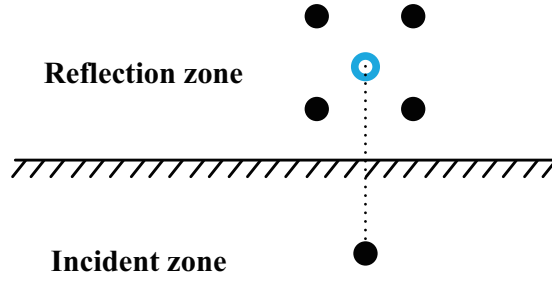


Figure 3: Templates for the integral weight (the solid points represent discrete velocity points, and the hollow points represent mirror points of discrete velocity points).

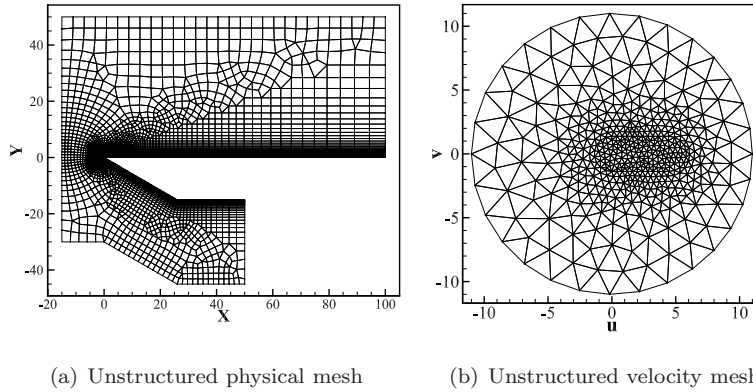


Figure 4: The physical mesh and velocity mesh used for supersonic flows passing a flat plate ($Ma=4.89$, $Kn=0.0078$, $T_\infty=116$ K, $T_w=290$ K).

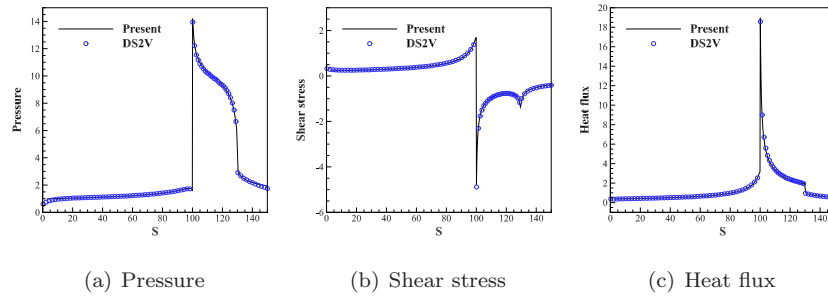


Figure 5: The physical quantity distribution on a flat plate surface: $\sigma=1$ ($Ma=4.89$, $Kn=0.0078$, $T_\infty=116$ K, $T_w=290$ K).

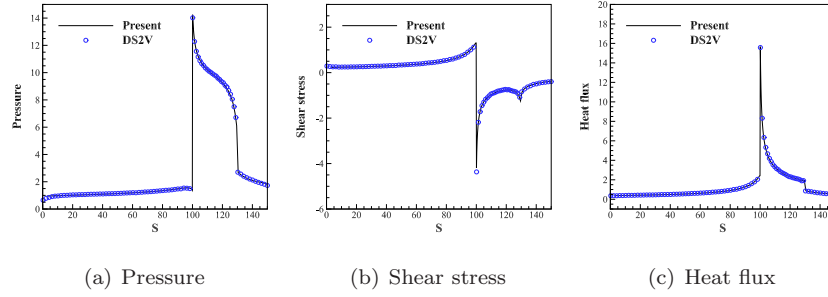


Figure 6: The physical quantity distribution on a flat plate surface: $\sigma=0.8$ ($Ma=4.89$, $Kn=0.0078$, $T_\infty=116$ K, $T_w=290$ K).

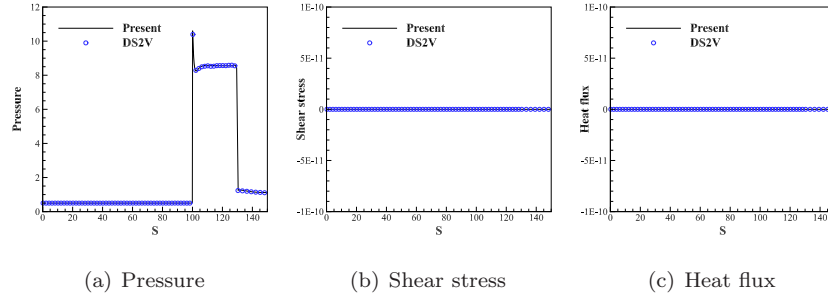


Figure 7: The physical quantity distribution on a flat plate surface: $\sigma=0$ ($Ma=4.89$, $Kn=0.0078$, $T_\infty=116$ K, $T_w=290$ K).

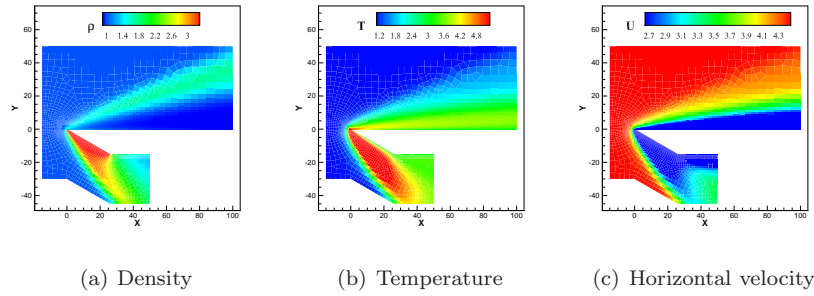


Figure 8: The results of supersonic flow over a flat plate with diffuse wall ($Ma=4.89$, $Kn=0.0078$, $T_\infty=116$ K, $T_w=290$ K).

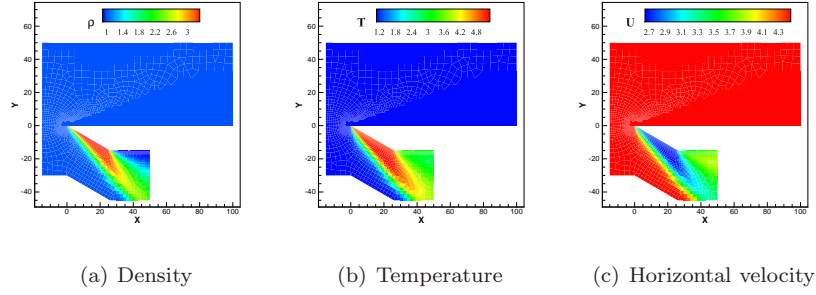


Figure 9: The results of supersonic flow over a flat plate with specular wall ($Ma=4.89$, $Kn=0.0078$, $T_\infty=116$ K, $T_w=290$ K).

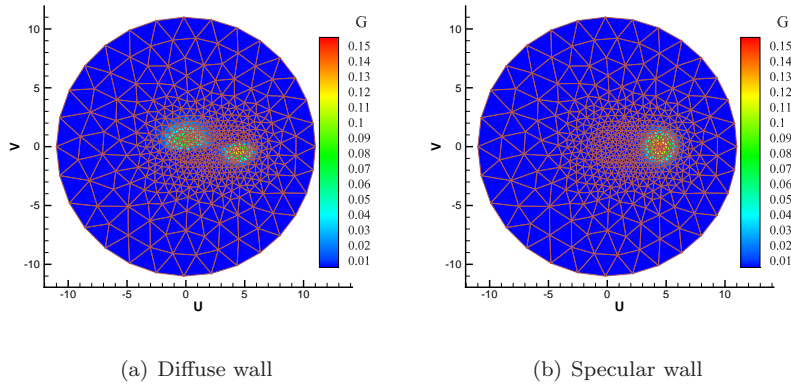
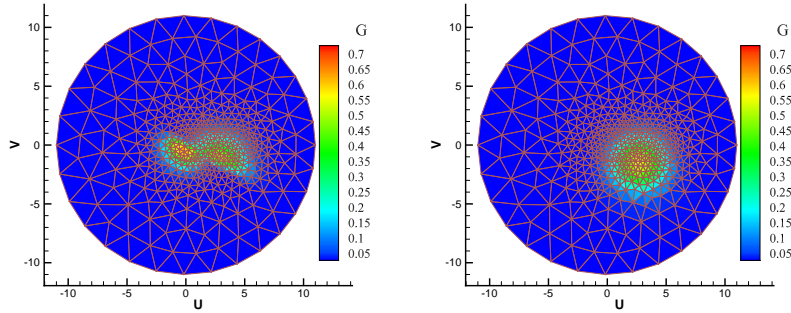


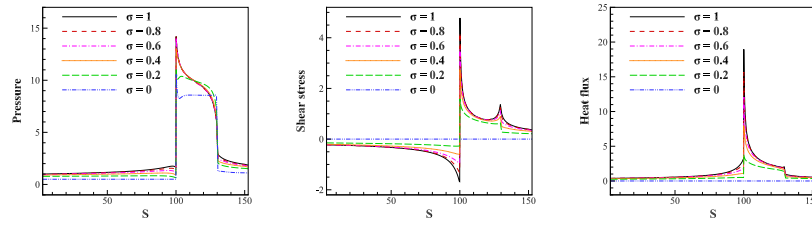
Figure 10: The distribution function on the top surface of the flat ($Ma=4.89$, $Kn=0.0078$, $T_\infty=116$ K, $T_w=290$ K).



(a) Diffuse wall

(b) Specular wall

Figure 11: The distribution function on the level of the flat ($Ma=4.89$, $Kn=0.0078$, $T_\infty=116$ K, $T_w=290$ K).



(a) Pressure

(b) Shear stress

(c) Heat flux

Figure 12: The physical quantity distribution on a flat plate surface at different σ ($Ma=4.89$, $Kn=0.0078$, $T_\infty=116$ K, $T_w=290$ K).

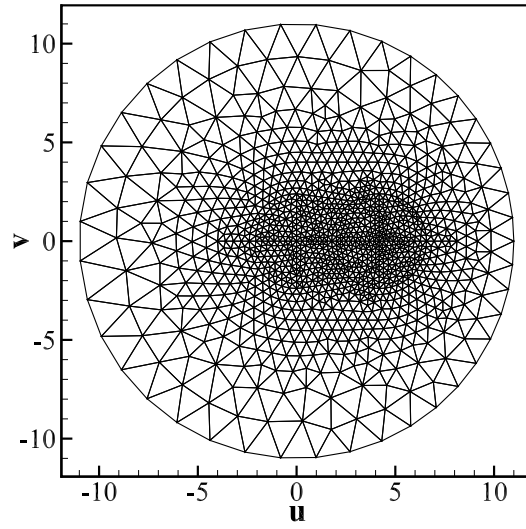


Figure 13: The velocity mesh used for supersonic flow over a cylinder ($Ma=5.0$, $Kn=1.0$, $T_\infty=273$ K, $T_w=273$ K).

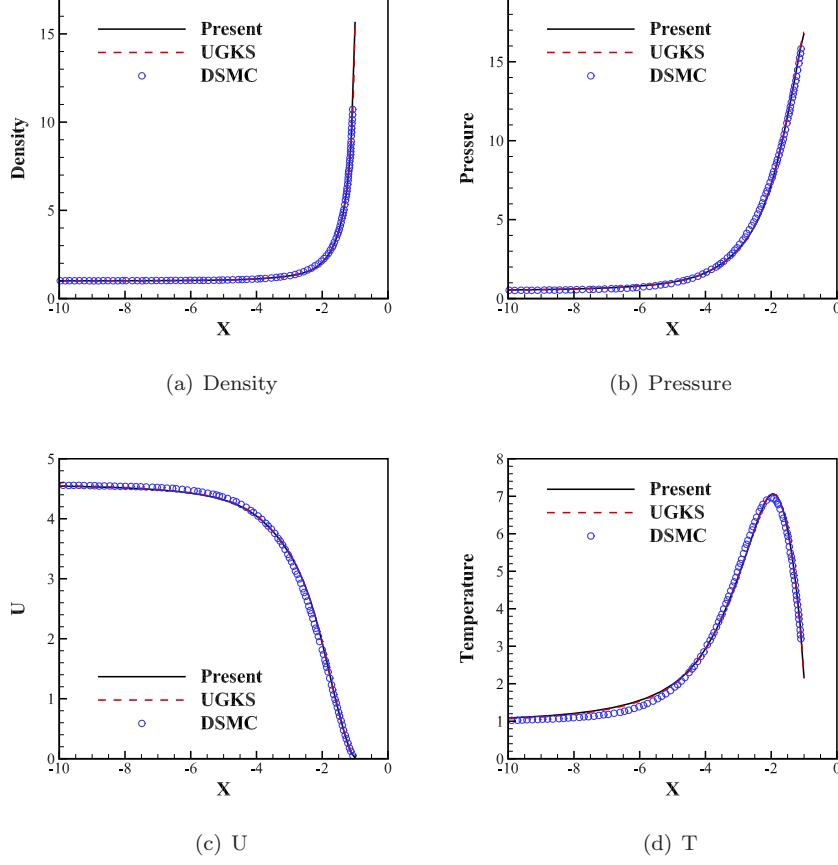


Figure 14: The physical quantity distribution on the stationary line in front of the cylinder at $\sigma=1$ ($Ma=5.0$, $Kn=1.0$, $T_\infty=273$ K, $T_w=273$ K).

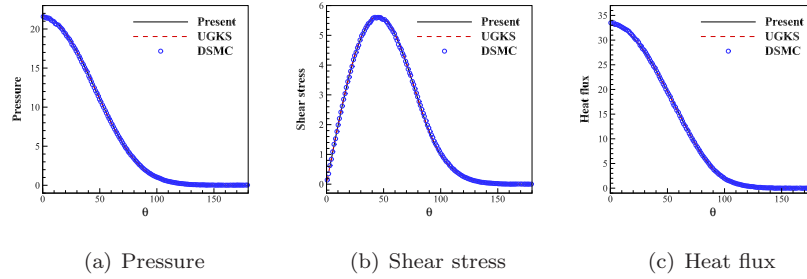
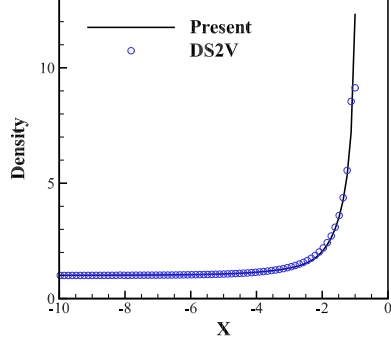
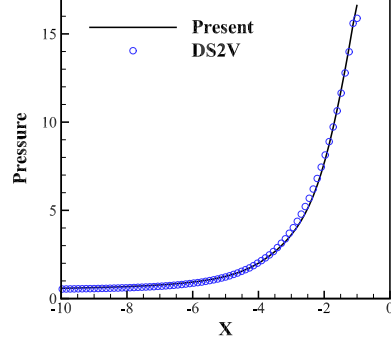


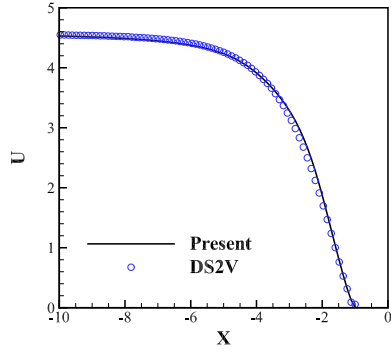
Figure 15: The physical quantity distribution on a cylinder surface at $\sigma=1$ ($Ma=5.0$, $Kn=1.0$, $T_\infty=273$ K, $T_w=273$ K).



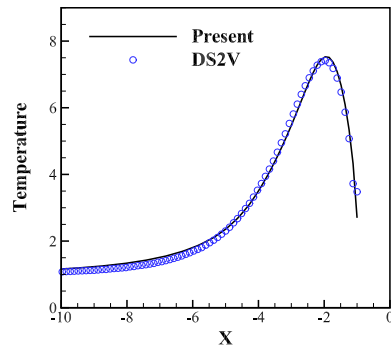
(a) Density



(b) Pressure

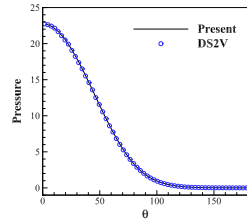


(c) U

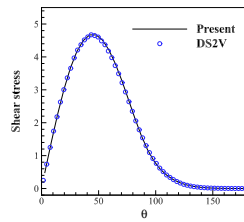


(d) T

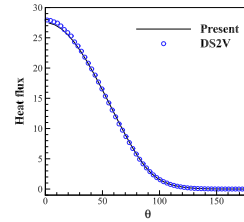
Figure 16: The physical quantity distribution on the stationary line in front of the cylinder at $\sigma=0.8$ ($Ma=5.0$, $Kn=1.0$, $T_\infty=273$ K, $T_w=273$ K).



(a) Pressure



(b) Shear stress



(c) Heat flux

Figure 17: The physical quantity distribution on a cylinder surface at $\sigma=0.8$ ($Ma=5.0$, $Kn=1.0$, $T_\infty=273$ K, $T_w=273$ K).

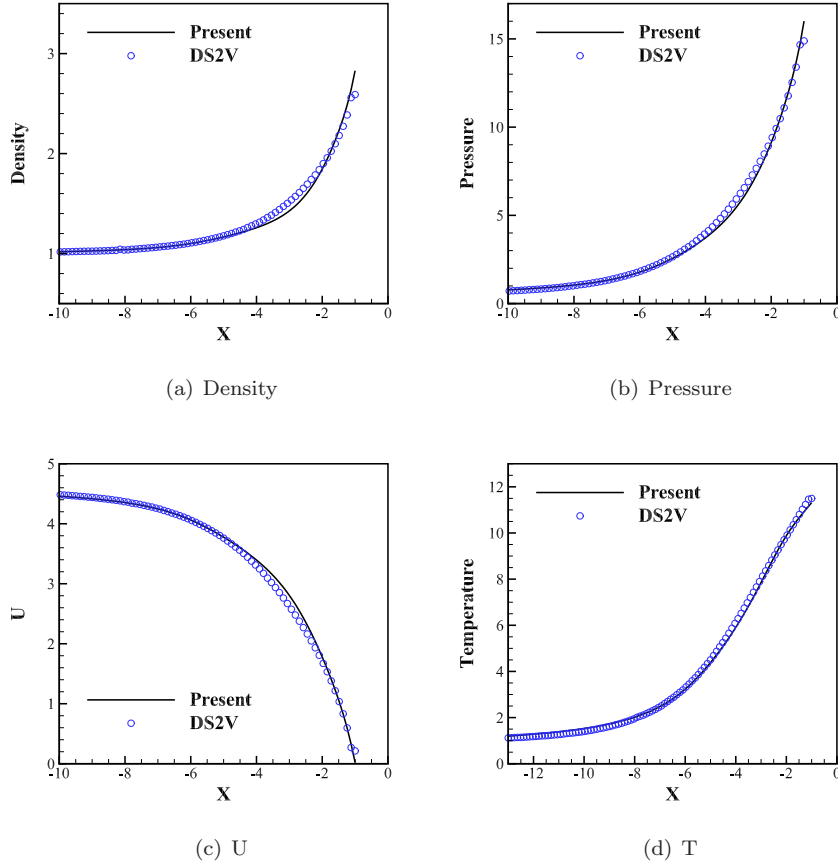


Figure 18: The physical quantity distribution on the stationary line in front of the cylinder at $\sigma=0$ ($Ma=5.0$, $Kn=1.0$, $T_\infty=273$ K, $T_w=273$ K).

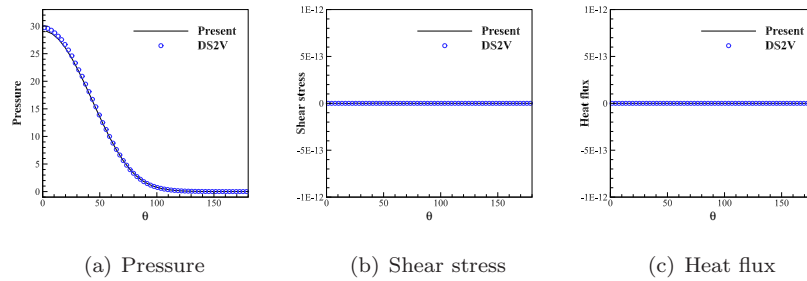


Figure 19: The physical quantity distribution on the cylinder surface at $\sigma=0$ ($Ma=5.0$, $Kn=1.0$, $T_\infty=273$ K, $T_w=273$ K).

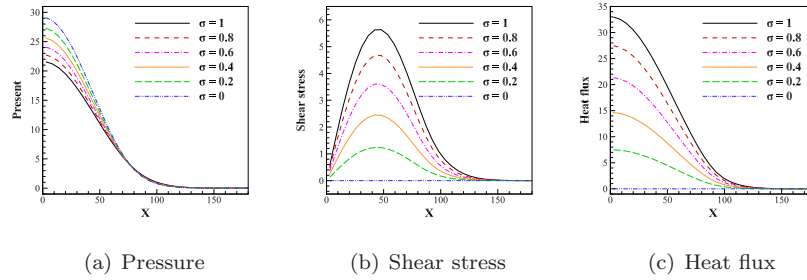


Figure 20: The physical quantity distribution on a cylinder surface at different σ ($Ma=5.0$, $Kn=1.0$, $T_\infty=273$ K, $T_w=273$ K).

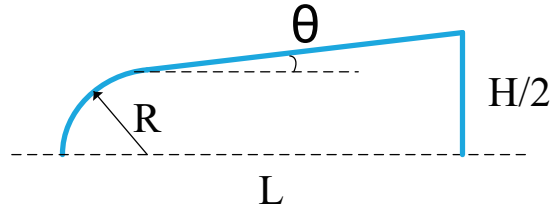


Figure 21: Geometric of blunt wedge (half-model).

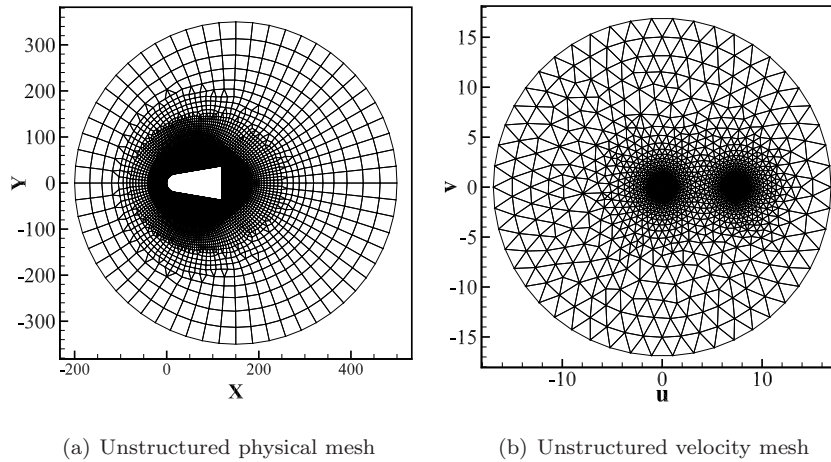


Figure 22: The physical mesh and velocity mesh used for hypersonic flows passing a blunt wedge ($Ma=8.1$, $Kn=0.338$, $T_\infty=189$ K, $T_w=273$ K).

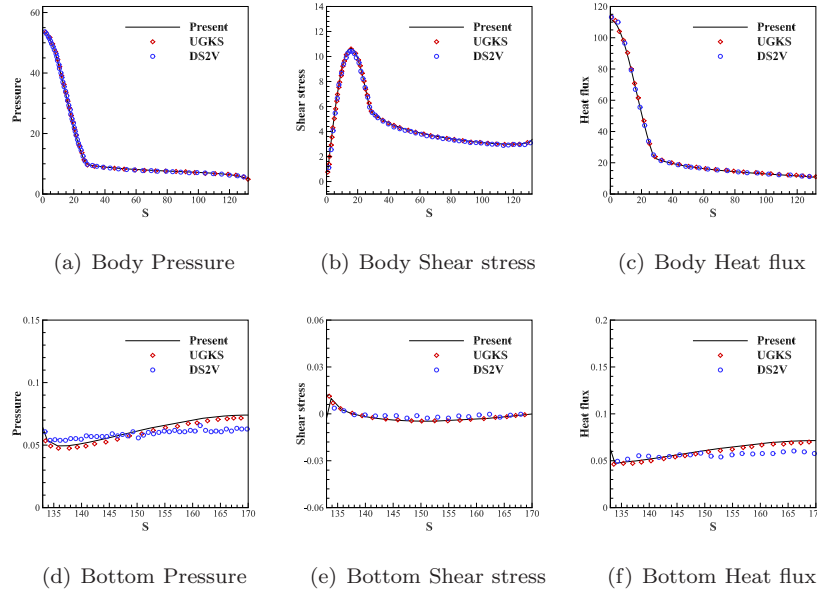


Figure 23: The physical quantity distribution on a blunt wedge surface at $\sigma=1$ ($Ma=8.1$, $Kn=0.338$, $T_\infty=189$ K, $T_w=273$ K).

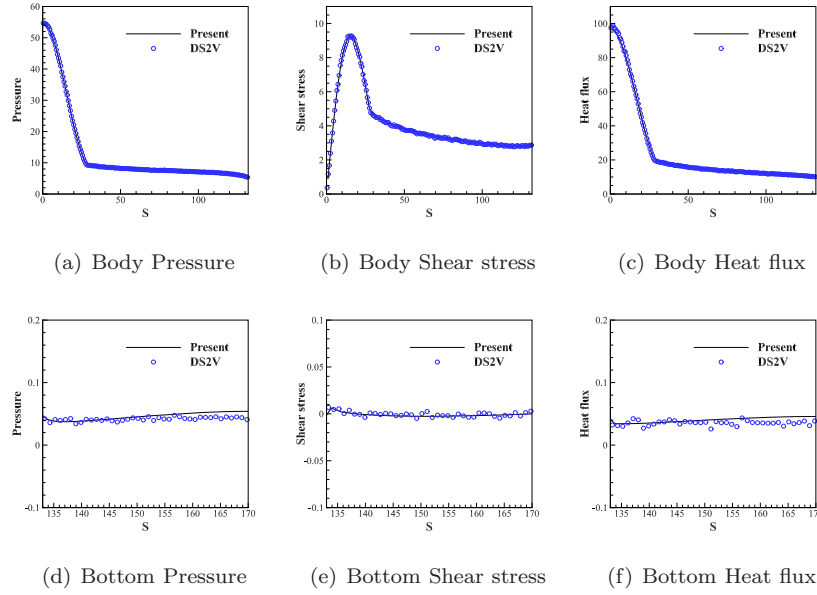


Figure 24: The physical quantity distribution on a blunt wedge surface at $\sigma=0.8$ ($Ma=8.1$, $Kn=0.338$, $T_\infty=189$ K, $T_w=273$ K).

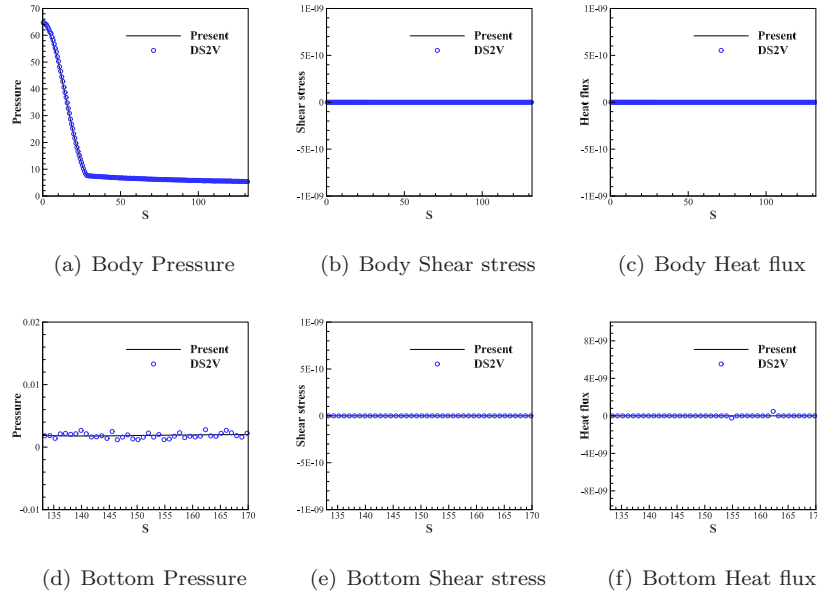


Figure 25: The physical quantity distribution on a blunt wedge surface at $\sigma=0$ ($Ma=8.1$, $Kn=0.338$, $T_\infty=189$ K, $T_w=273$ K).

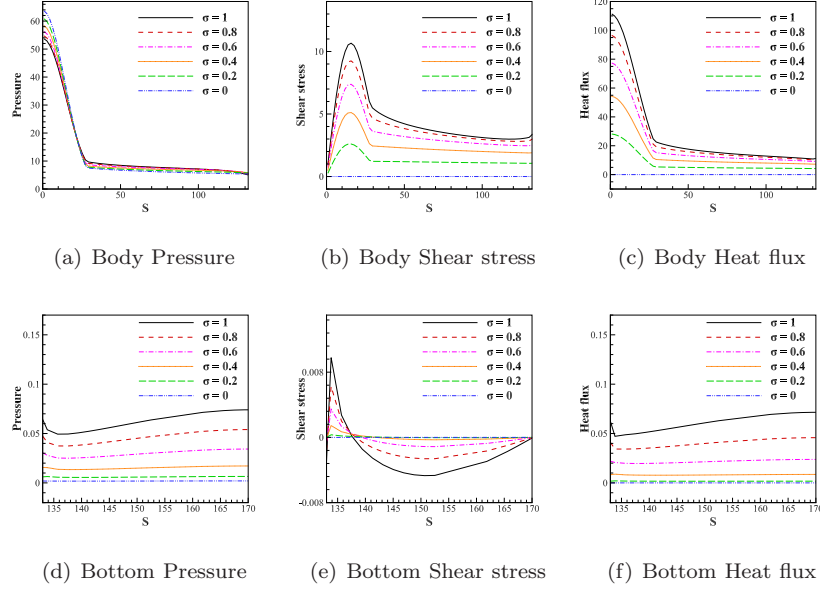


Figure 26: The physical quantity distribution on a blunt wedge surface at different σ ($Ma=8.1$, $Kn=0.338$, $T_\infty=189$ K, $T_w=273$ K).

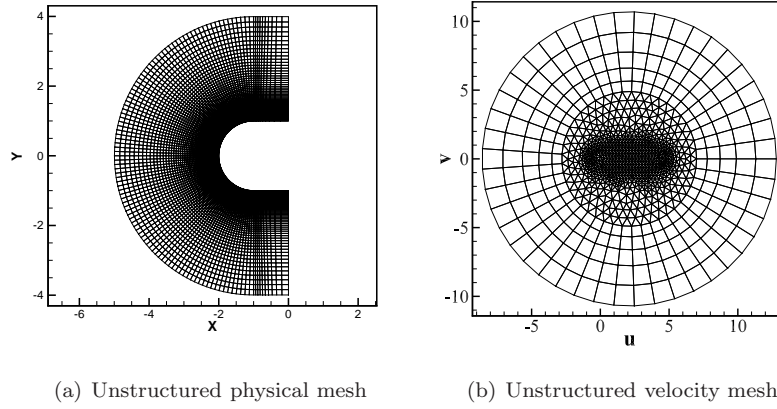


Figure 27: The physical mesh and velocity mesh used for hypersonic flows passing a blunt circular cylinder ($Ma=5.0$, $Kn=0.1$, $T_\infty=273$ K, $T_w=273$ K).

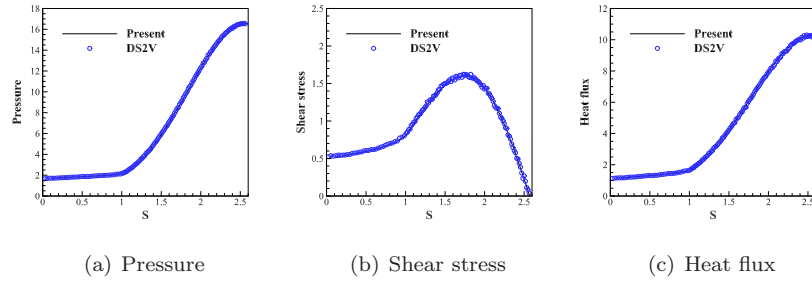


Figure 28: The physical quantity distribution on a blunt circular cylinder surface at $\sigma=1$ ($Ma=5.0$, $Kn=0.1$, $T_\infty=273$ K, $T_w=273$ K).

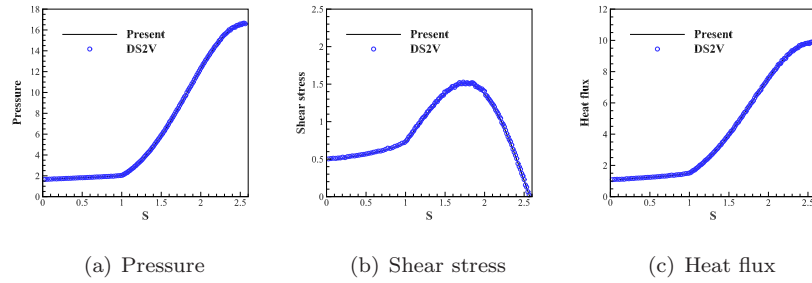


Figure 29: The physical quantity distribution on a blunt circular cylinder surface at $\sigma=0.8$ ($Ma=5.0$, $Kn=0.1$, $T_\infty=273$ K, $T_w=273$ K).

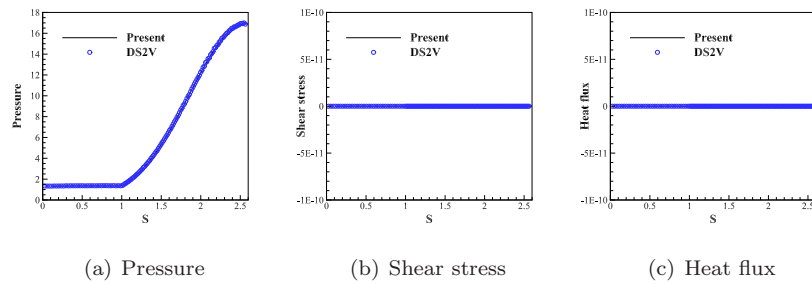


Figure 30: The physical quantity distribution on a blunt circular cylinder surface at $\sigma=0$ ($Ma=5.0$, $Kn=0.1$, $T_\infty=273$ K, $T_w=273$ K).

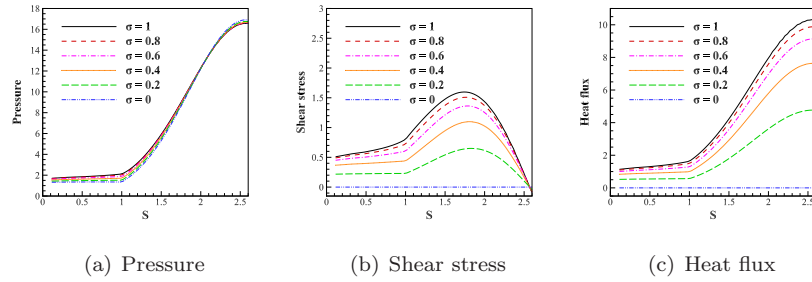


Figure 31: The physical quantity distribution on a blunt circular cylinder surface at different σ ($Ma=5.0$, $Kn=0.1$, $T_\infty=273$ K, $T_w=273$ K).

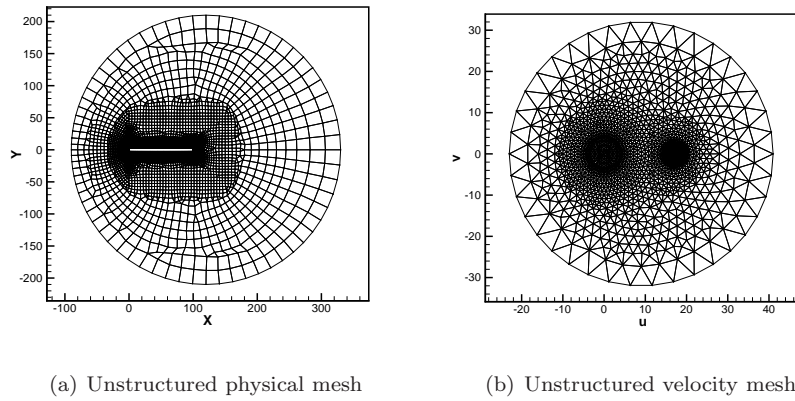


Figure 32: The physical mesh and velocity mesh used for rarefied hypersonic flows over a flat plate ($Ma=20.2$, $Kn=0.0169$, $T_\infty=13.32$ K, $T_w=290$ K).

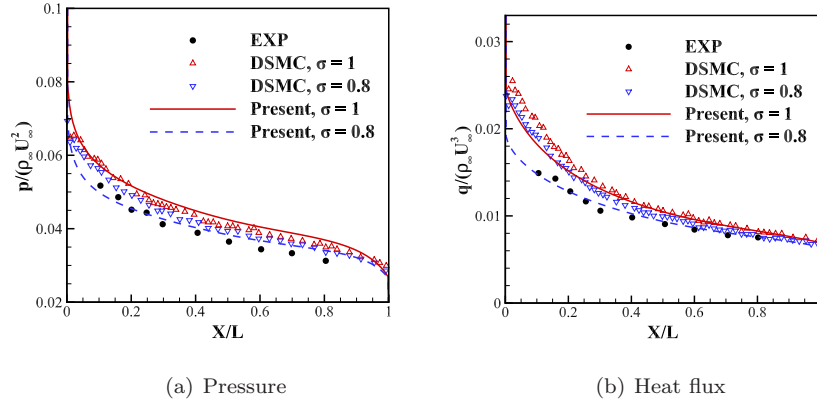


Figure 33: The distribution of pressure and heat flux on the plate's lower surface at an attack angle of 0 degree ($Ma=20.2$, $Kn=0.0169$, $T_\infty=13.32$ K, $T_w=290$ K).

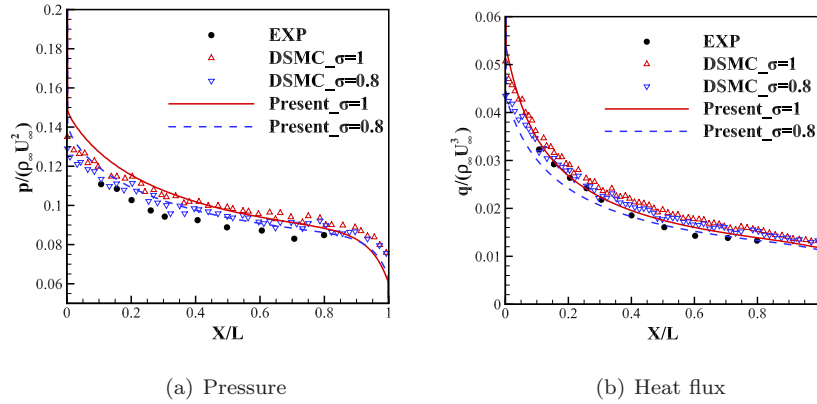


Figure 34: The distribution of pressure and heat flux on the plate's lower surface at an attack angle of 10 degrees ($Ma=20.2$, $Kn=0.0169$, $T_\infty=13.32$ K, $T_w=290$ K).

References

[1] G. A. Bird, Molecular gas dynamics and the direct simulation of gas flows, Molecular gas dynamics and the direct simulation of gas flows (1994).

470 [2] S. Chen, K. Xu, C. Lee, Q. Cai, A unified gas kinetic scheme with moving

- mesh and velocity space adaptation, *Journal of Computational Physics* 231 (20) (2012) 6643–6664.
- [3] L. Zhu, Z. Guo, K. Xu, Discrete unified gas kinetic scheme on unstructured meshes, *Computers & Fluids* 127 (2016) 211–225.
- 475 [4] T. E. Schwartzentruber, I. D. Boyd, A hybrid particle-continuum method applied to shock waves, *Journal of Computational Physics* 215 (2) (2006) 402–416.
- [5] T. E. Schwartzentruber, L. C. Scalabrin, I. D. Boyd, Hybrid particle-continuum simulations of hypersonic flow over a hollow-cylinder-flare geometry, *AIAA journal* 46 (8) (2008) 2086–2095.
- 480 [6] J. M. Burt, I. D. Boyd, A hybrid particle approach for continuum and rarefied flow simulation, *Journal of Computational Physics* 228 (2) (2009) 460–475.
- [7] Q. Sun, I. D. Boyd, G. V. Candler, A hybrid continuum/particle approach for modeling subsonic, rarefied gas flows, *Journal of Computational Physics* 194 (1) (2004) 256–277.
- 485 [8] T. E. Schwartzentruber, L. C. Scalabrin, I. D. Boyd, A modular particle-continuum numerical method for hypersonic non-equilibrium gas flows, *Journal of Computational Physics* 225 (1) (2007) 1159–1174.
- 490 [9] S. Jin, Efficient asymptotic-preserving (ap) schemes for some multiscale kinetic equations, *SIAM Journal on Scientific Computing* 21 (2) (1999) 441–454.
- [10] K. Xu, J.-C. Huang, A unified gas-kinetic scheme for continuum and rarefied flows, *Journal of Computational Physics* 229 (20) (2010) 7747–7764.
- 495 [11] K. Xu, *Direct modeling for computational fluid dynamics: construction and application of unified gas-kinetic schemes*, Vol. 4, World Scientific, 2014.

- [12] Z. Guo, K. Xu, R. Wang, Discrete unified gas kinetic scheme for all knudsen number flows: Low-speed isothermal case, *Physical Review E* 88 (3) (2013) 033305.
- 500 [13] Z. Guo, R. Wang, K. Xu, Discrete unified gas kinetic scheme for all knudsen number flows. ii. thermal compressible case, *Physical Review E* 91 (3) (2015) 033313.
- [14] W. Sun, S. Jiang, K. Xu, A multidimensional unified gas-kinetic scheme for radiative transfer equations on unstructured mesh, *Journal of Computational Physics* 351 (2017) 455–472.
- 505 [15] Y. Wang, C. Zhong, S. Liu, et al., Arbitrary lagrangian-eulerian-type discrete unified gas kinetic scheme for low-speed continuum and rarefied flow simulations with moving boundaries, *Physical Review E* 100 (6) (2019) 063310.
- 510 [16] S. Chen, C. Zhang, L. Zhu, Z. Guo, A unified implicit scheme for kinetic model equations. part i. memory reduction technique, *Science bulletin* 62 (2) (2017) 119–129.
- [17] Y. Zhu, C. Liu, C. Zhong, K. Xu, Unified gas-kinetic wave-particle methods. ii. multiscale simulation on unstructured mesh, *Physics of Fluids* 31 (6) (2019) 067105.
- 515 [18] Y. Zhu, C. Zhong, K. Xu, Implicit unified gas-kinetic scheme for steady state solutions in all flow regimes, *Journal of Computational Physics* 315 (2016) 16–38.
- [19] R. Yuan, C. Zhong, A conservative implicit scheme for steady state solutions of diatomic gas flow in all flow regimes, *Computer Physics Communications* 247 (2020) 106972.
- 520 [20] W. Sun, S. Jiang, K. Xu, An implicit unified gas kinetic scheme for radiative transfer with equilibrium and non-equilibrium diffusive limits, *Communications in Computational Physics* 22 (4) (2017) 889–912.

- 525 [21] Q. Zhang, Y. Wang, D. Pan, J. Chen, S. Liu, C. Zhuo, C. Zhong, Unified x-space parallelization algorithm for conserved discrete unified gas kinetic scheme, *Computer Physics Communications* 278 (2022) 108410.
- [22] S. Chen, Z. Guo, K. Xu, Simplification of the unified gas kinetic scheme, *Physical Review E* 94 (2) (2016) 023313.
- 530 [23] S. Liu, C. Zhong, Modified unified kinetic scheme for all flow regimes, *Physical Review E* 85 (6) (2012) 066705.
- [24] M. Zhong, S. Zou, D. Pan, C. Zhuo, C. Zhong, A simplified discrete unified gas kinetic scheme for incompressible flow, *Physics of Fluids* 32 (9) (2020) 093601.
- 535 [25] M. Zhong, S. Zou, D. Pan, C. Zhuo, C. Zhong, A simplified discrete unified gas-kinetic scheme for compressible flow, *Physics of Fluids* 33 (3) (2021) 036103.
- [26] L. Zhu, Z. Guo, Numerical study of nonequilibrium gas flow in a microchannel with a ratchet surface, *Physical Review E* 95 (2) (2017) 023113.
- 540 [27] R. Zhang, S. Liu, C. Zhong, C. Zhuo, Unified gas-kinetic scheme with simplified multi-scale numerical flux for thermodynamic non-equilibrium flow in all flow regimes, arXiv preprint arXiv:2208.14599 (2022).
- [28] Z. Yang, C. Zhong, C. Zhuo, et al., Phase-field method based on discrete unified gas-kinetic scheme for large-density-ratio two-phase flows, *Physical*
545 *Review E* 99 (4) (2019) 043302.
- [29] S. Tao, H. Zhang, Z. Guo, L.-P. Wang, A combined immersed boundary and discrete unified gas kinetic scheme for particle-fluid flows, *Journal of Computational Physics* 375 (2018) 498–518.
- 550 [30] Y. Zhang, L. Zhu, R. Wang, Z. Guo, Discrete unified gas kinetic scheme for all knudsen number flows. iii. binary gas mixtures of maxwell molecules, *Physical Review E* 97 (5) (2018) 053306.

- [31] W. Sun, S. Jiang, K. Xu, An asymptotic preserving unified gas kinetic scheme for gray radiative transfer equations, *Journal of Computational Physics* 285 (2015) 265–279.
- 555 [32] Z. Guo, K. Xu, Discrete unified gas kinetic scheme for multiscale heat transfer based on the phonon boltzmann transport equation, *International Journal of Heat and Mass Transfer* 102 (2016) 944–958.
- [33] D. Pan, C. Zhong, C. Zhuo, W. Tan, A unified gas kinetic scheme for transport and collision effects in plasma, *Applied Sciences* 8 (5) (2018) 746.
- 560 [34] T. Shuang, S. Wenjun, W. Junxia, N. Guoxi, A parallel unified gas kinetic scheme for three-dimensional multi-group neutron transport, *Journal of Computational Physics* 391 (2019) 37–58.
- [35] C. Liu, Z. Wang, K. Xu, A unified gas-kinetic scheme for continuum and rarefied flows vi: Dilute disperse gas-particle multiphase system, *Journal of Computational Physics* 386 (2019) 264–295.
- 565 [36] P. Wang, L.-P. Wang, Z. Guo, Comparison of the lattice boltzmann equation and discrete unified gas-kinetic scheme methods for direct numerical simulation of decaying turbulent flows, *Physical Review E* 94 (4) (2016) 043304.
- 570 [37] R. Zhang, C. Zhong, S. Liu, C. Zhuo, Large-eddy simulation of wall-bounded turbulent flow with high-order discrete unified gas-kinetic scheme, *Advances in Aerodynamics* 2 (1) (2020) 1–27.
- [38] V. Titarev, Numerical modeling of high-speed rarefied gas flows over blunt bodies using model kinetic equations, *European Journal of Mechanics-B/Fluids* 64 (2017) 112–117.
- 575 [39] C. Baranger, J. Claudel, N. Hérouard, L. Mieussens, Locally refined discrete velocity grids for deterministic rarefied flow simulations, in: AIP

- Conference Proceedings, Vol. 1501, American Institute of Physics, 2012,
580 pp. 389–396.
- [40] R. R. Arslanbekov, V. I. Kolobov, A. A. Frolova, Kinetic solvers with adaptive mesh in phase space, *Physical Review E* 88 (6) (2013) 063301.
- [41] J. Chen, S. Liu, Y. Wang, C. Zhong, Conserved discrete unified gas-kinetic scheme with unstructured discrete velocity space, *Physical Review*
585 *E* 100 (4) (2019) 043305.
- [42] J. Chen, S. Liu, Y. Wang, C. Zhong, A compressible conserved discrete unified gas-kinetic scheme with unstructured discrete velocity space for multi-scale jet flow expanding into vacuum environment, *Commun. Comput. Phys* 28 (2020) 1502–1535.
- 590 [43] W. Santos, M. Lewis, Dsmc calculations of rarefied hypersonic flow over power law leading edges with incomplete surface accommodation, in: 34th AIAA Fluid Dynamics Conference and Exhibit, 2004, p. 2636.
- [44] E. H. Kennard, et al., *Kinetic theory of gases*, Vol. 483, McGraw-hill New York, 1938.
- 595 [45] X. Jin, B. Wang, X. Cheng, Q. Wang, F. Huang, The effects of maxwellian accommodation coefficient and free-stream knudsen number on rarefied hypersonic cavity flows, *Aerospace Science and Technology* 97 (2020) 105577.
- [46] J. C. Maxwell, Vii. on stresses in rarified gases arising from inequalities of temperature, *Philosophical Transactions of the royal society of London* (170) (1879) 231–256.
600
- [47] B.-Y. Cao, J. Sun, M. Chen, Z.-Y. Guo, Molecular momentum transport at fluid-solid interfaces in mems/nems: a review, *International journal of molecular sciences* 10 (11) (2009) 4638–4706.
- [48] C. Cercignani, M. Lampis, Kinetic models for gas-surface interactions,
605 *Transport theory and statistical physics* 1 (2) (1971) 101–114.

- [49] R. Lord, Some extensions to the cercignani–lampis gas–surface scattering kernel, *Physics of Fluids A: Fluid Dynamics* 3 (4) (1991) 706–710.
- [50] R. Lord, Some further extensions of the cercignani–lampis gas–surface interaction model, *Physics of Fluids* 7 (5) (1995) 1159–1161.
- 610 [51] S. Nocilla, The surface re-emission law in free molecule flow (1962).
- [52] F. Hurlbut, F. Sherman, Application of the nocilla wall reflection model to free-molecule kinetic theory, *The Physics of Fluids* 11 (3) (1968) 486–496.
- [53] D. C. Wadsworth, D. B. VanGilder, V. K. Dogra, Gas-surface interaction model evaluation for dsmc applications, in: *AIP Conference Proceedings*, Vol. 663, American Institute of Physics, 2003, pp. 965–972.
- 615 [54] M. O. Hedahl, R. G. Wilmoth, Comparisons of the maxwell and cll gas/surface interaction models using dsmc, Tech. rep. (1995).
- [55] N. Yamanishi, Y. Matsumoto, K. Shobatake, Multistage gas-surface interaction model for the direct simulation monte carlo method, *Physics of Fluids* 11 (11) (1999) 3540–3552.
- 620 [56] Y.-D. Zhang, A.-G. Xu, G.-C. Zhang, Z.-H. Chen, Discrete boltzmann method with maxwell-type boundary condition for slip flow, *Communications in Theoretical Physics* 69 (1) (2018) 77.
- [57] C. Lim, C. Shu, X. Niu, Y. Chew, Application of lattice boltzmann method to simulate microchannel flows, *Physics of fluids* 14 (7) (2002) 2299–2308.
- 625 [58] P. L. Bhatnagar, E. P. Gross, M. Krook, A model for collision processes in gases. i. small amplitude processes in charged and neutral one-component systems, *Physical review* 94 (3) (1954) 511.
- [59] E. Shakhov, Generalization of the krook kinetic relaxation equation, *Fluid dynamics* 3 (5) (1968) 95–96.
- 630

- [60] L. H. Holway Jr, New statistical models for kinetic theory: methods of construction, *The physics of fluids* 9 (9) (1966) 1658–1673.
- [61] V. Rykov, A model kinetic equation for a gas with rotational degrees of freedom, *Fluid Dynamics* 10 (6) (1975) 959–966.
- 635 [62] J. Yang, J. Huang, Rarefied flow computations using nonlinear model boltzmann equations, *Journal of Computational Physics* 120 (2) (1995) 323–339.
- [63] H. Liu, Y. Cao, Q. Chen, M. Kong, L. Zheng, A conserved discrete unified gas kinetic scheme for microchannel gas flows in all flow regimes, *Computers & Fluids* 167 (2018) 313–323.
- 640 [64] V. Venkatakrishnan, Convergence to steady state solutions of the euler equations on unstructured grids with limiters, *Journal of Computational Physics* 118 (1) (1995) 120–130.
- [65] Z. Guo, K. Xu, Progress of discrete unified gas-kinetic scheme for multiscale flows, *Advances in Aerodynamics* 3 (1) (2021) 1–42.
- 645 [66] N. Tsuboi, Y. Matsumoto, Experimental and numerical study of hypersonic rarefied gas flow over flat plates, *AIAA journal* 43 (6) (2005) 1243–1255.
- [67] S. Liu, C. Zhong, Investigation of the kinetic model equations, *Physical Review E* 89 (3) (2014) 033306.
- [68] D. Jiang, M. Mao, J. Li, X. Deng, An implicit parallel ugks solver for flows covering various regimes, *Advances in Aerodynamics* 1 (1) (2019) 1–24.
- 650 [69] J. Davis, J. Harvey, Comparison of the direct simulated method with experiment for rarefied flat plate flow, *Progress in Astronautics and Aeronautics* (1963) 335–348.
- [70] J. Allegre, M. Raffin, A. Chpoun, L. Gottesdiener, Rarefied hypersonic flow over a flat plate with truncated leading edge, *Rarefied gas dynamics: Space science and engineering* (1994) 285–295.
- 655

- [71] N. Tsuboi, H. Yamaguchi, Y. Matsumoto, Direct simulation monte carlo method on rarefied hypersonic gas flow around flat plates, *Journal of spacecraft and rockets* 41 (3) (2004) 397–405.
- 660 [72] R. C. Palharini, C. White, T. J. Scanlon, R. E. Brown, M. K. Borg, J. M. Reese, Benchmark numerical simulations of rarefied non-reacting gas flows using an open-source dsmc code, *Computers & Fluids* 120 (2015) 140–157.
- [73] D. J. Rader, J. N. Castaneda, J. R. Torczynski, T. W. Grasser, W. M. Trott, Measurements of thermal accommodation coefficients., Tech. rep.,
665 Sandia National Laboratories (SNL), Albuquerque, NM, and Livermore, CA (2005).
- [74] W. M. Trott, J. N. Castañeda, J. R. Torczynski, M. A. Gallis, D. J. Rader, An experimental assembly for precise measurement of thermal accommodation coefficients, *Review of scientific instruments* 82 (3) (2011) 035120.
- 670 [75] M. Schouler, Y. Prévèreaud, L. Mieussens, Survey of flight and numerical data of hypersonic rarefied flows encountered in earth orbit and atmospheric reentry, *Progress in Aerospace Sciences* 118 (2020) 100638.